

Department of Physics and Astronomy
University of Heidelberg

Master thesis
in Physics
submitted by
Arthur Schönhals
born in Tomsk

2013

Imaging of ultracold Cesium atoms at high magnetic fields

This master thesis has been carried out by *Arthur Schönhals* at the
Physikalisches Institut
under the supervision of
Prof. Dr. Matthias Weidemüller

Abbildung von ultrakalten Cäsiumatomen bei hohen Magnetfeldern

Die vorliegende Arbeit beschreibt den Aufbau und die erfolgreiche Umsetzung eines Systems zur Absorptionsabbildung von ultrakalten Cäsiumatomen in äußeren Magnetfeldern im Bereich von 0 bis 1000 G. Das neue System besteht aus zwei DBR-Lasern mit einem großen durchstimmbaren Frequenzbereich von ~ 27 GsHz, die zum Abbilden und zum Rückpumpen von Atomen verwendet werden. Beide sind über *frequency offset locking* stabilisiert, sodass der gesamte Bereich der Magnetfeld-induzierten Frequenzverschiebungen des entsprechenden Überganges abgedeckt ist. Der Lock weist eine Stabilität von ~ 1 MHz über 10 min auf und das Frequenzrauschen ist vorwiegend durch die Laserlinienbreite von ~ 6 MHz bzw. ~ 14 MHz dominiert. Der Einfluss der Linienbreite zeigt sich auch durch eine verringerte optische Dichte bei Absorptionsabbildungen an Atomen. Durch einen Vergleich mit dem bisherigen Abbildungssystem bei Nullfeld konnte ein Korrekturterm von $C_{\text{corr}} \approx 1.53(4)$ zur Bestimmung der Atomzahl ermittelt werden. Zudem wurde gezeigt, dass ultrakalte Cäsiumatome bis zu 1000 G optisch abgebildet werden können.

Imaging of ultracold cesium atoms at high magnetic fields

The present work describes the development and successful implementation of a system for absorption imaging of ultracold cesium atoms in external magnetic fields ranging from 0 to 1000 G. The new setup consists of two DBR lasers with a large tunable frequency range of ~ 27 GHz, which are used for imaging and repumping atoms. Both are stabilized by *frequency offset locking*, which covers the entire range of magnetic-field induced frequency shifts of the corresponding transition. The lock features a stability of ~ 1 MHz over 10 min and the frequency noise is mainly dominated by the laser linewidths of ~ 6 MHz and ~ 14 MHz. The influence of the linewidth results also in a reduced optical density during absorption imaging of atoms. By comparing with the previous imaging system at zero field a correction term of $C_{\text{corr}} \approx 1.53(4)$ could be obtained for determination of the atom number. Moreover, we demonstrated optical absorption imaging of ultracold Cs atoms up to 1000 G.

Contents

1	Introduction	1
2	Cesium at high magnetic fields	5
2.1	Hyperfine structure of cesium	5
2.2	Interaction of cesium atoms with an external magnetic field	7
2.3	Optical cycling transitions	10
3	High-field imaging system	17
3.1	Laser system	17
3.1.1	DBR laser	18
3.1.2	Locking Scheme	20
3.1.3	Optical setup	22
3.2	Frequency offset locking	24
3.2.1	Principle of offset locking	24
3.2.2	Setup for offset locking	27
3.2.3	Stability and noise	31
4	Absorption imaging of Cesium atoms	41
4.1	Absorption imaging	41
4.2	Comparison with a reference system	48
4.3	Imaging at high magnetic fields	52
5	Conclusion and outlook	57
Appendix		59
A	Atomic properties of Cs	60
B	Frequency offset lock with a narrow-band laser	63
C	Modulation transfer spectroscopy	69
D	Detailed overview of optical setup	73

Bibliography 75

Danksagungen 81

1. Introduction

In the last thirty years, the field of quantum gases evolved into an important and large field of atomic physics. Since it became possible to control atomic degrees of freedom and the interaction between atoms precisely, quantum gases offer an experimental simulation of theoretically predicted phenomena. The initiation for this development was the invention of laser cooling in 1982 [1], which was a pre-stage for the preparation of atoms at ultracold temperatures close to absolute zero. The first evidence for quantum degeneracy was given by the experimental realization of a Bose-Einstein condensate (BEC) [2, 3] in a dilute alkali vapor in 1995 [4, 5, 6]. Few years later a degenerate Fermi gas with ^{40}K atoms and ^6Li was demonstrated [7, 8, 9]. Based on these achievements, new techniques as for example optical dipole traps (ODT) [10] were developed, that advanced the investigation of further effects like the observation of molecular condensation of paired fermions [11, 12, 13]. This milestone in the progress of quantum gases could not be achieved without the development of the ability to manipulate and control the interaction strength between atoms by Feshbach resonances [14, 15], which considerably expanded the field of ultracold quantum gases. In this context, interspecies Feshbach resonances, especially between alkaline-metal species [16, 17, 18, 19], became of particular interest, since they offer a wide range for the investigation of different quantum phenomena, e.g. in few- or many-body physics.

A promising candidate is the Li-Cs system. Our group succeeded to observe interspecies Feshbach resonances in a mixture of ultracold ^6Li and ^{133}Cs atoms [20]. Both species were exposed to a magnetic field while being simultaneously held in a crossed ODT at $T_{\text{Cs}} = 8 \mu\text{K}$ and $T_{\text{Li}} = 2 \mu\text{K}$, respectively, and measured by high-field absorption imaging of remaining Li atoms. All found Feshbach resonances are within the range of 650 - 950 G. The found s-wave resonances provide the opportunity to observe a variety of quantum phenomena.

A broad s-wave resonance at 889.2 G, for example, gives the possibility to observe polaron physics. At these fields Cs is almost non-interacting, due to a zero crossing at ~ 870 G of the Cs scattering length originating from a broad Cs s-wave Feshbach resonance

1 Introduction

at 787 G. Because of the Pauli exclusion principle spin-polarized Li is also non-interacting. Thus, a system could be realized that features tuning via the interspecies scattering length between Li and Cs, which represents promising a candidate to form polarons [21, 22, 23].

Moreover, the s-wave resonance at 889.2 G and another broad one at 843.5 G give access to the study of the universal Efimov effect[24]. The Efimov effect describes three-body states formed in the universal regime, which is achieved when the scattering length a (characterizes the two-body scattering), exceeds the range l of the inter-atomic potential, $|a| \gg l$ [25, 26]. In this regime all essential properties are described by the scattering length a , and a finite series of trimer states exists for a diverging scattering length $a \rightarrow \infty$. The series follows a universal geometrical and logarithmic scaling law $\kappa = e^{\pi/s_0}$ that only depends on the mass ratio (included in s_0). For identical bosons the scaling factor is $\kappa \approx 22.7$, but for the case of a mass imbalanced system as for $^{133}\text{Cs}_2 - {}^6\text{Li}$ trimers with a high mass ratio of $m_{\text{Cs}}/m_{\text{Li}} \approx 22$ the scaling reduces to $\kappa \approx 4.88$ [27]. This makes a Bose-Fermi mixture of Li and Cs atoms an optimal system for the observation of a series of Efimov states.

In order to fully characterize the processes involving the Efimov effect or to observe polaronic signatures, it is favourable to image both species at high magnetic fields. Because Li atoms may be faster evaporated away near the Feshbach resonances, the imaging of the much heavier Cs atoms could reveal clearer signatures. Until now Cs atoms could be imaged only at zero field, which means that the magnetic coils had to be switched off after every experimental cycle. This takes a certain time and yields to additional technical noise that influences the sensitivity of the detection (e.g. fringes on absorption images). To image atoms at high magnetic fields, the laser frequency has to be shifted by the same value as the frequency shift of the imaging transition, which is induced by the magnetic field. For field strengths up to ~ 1000 MHz the frequency shift is on the order of few GHz. For this reason a new imaging system for high magnetic fields has to fulfill some experimental requirements. First, a laser is needed, which provides a wide tunable frequency range covering the span of induced frequency shifts. Secondly, a laser stabilization is required, which allows to tune the laser frequency by few GHz. In the framework of this thesis such a high-field imaging system was assembled and characterized. It consists of two DBR lasers that are used for repumping and imaging of Cs atoms, featuring a tunable frequency range of ~ 27 GHz. They are stabilized by *frequency offset locking* [28, 29, 30], which provides tuning the laser frequencies in the range of the magnetic-field induced frequency shifts.

The thesis is structured as follows: Chapter 2 explains the behaviour of the energy structure of cesium in an external magnetic field. Moreover, this chapter reviews the

determination of suitable optical cycling transitions for repumping and imaging at high magnetic fields. In chapter 3 the high-field imaging system is specified, beginning with the description of the laser system and followed by the explanation and detailed characterization of the laser lock. In chapter 4 the new setup is first tested at zero field and characterized by means of comparing with the existing low-field imaging system in terms of absorption imaging of atoms at zero field. Finally, high-field imaging was tested successfully for magnetic fields up to 1000 G, which is presented in the second part of this chapter. The last chapter 5 concludes and gives an outlook for experiments, where high-field imaging is required.

2. Cesium at high magnetic fields

In an external magnetic field the description of the atomic hyperfine structure requires additional quantum numbers, opposed to the situation without an external magnetic field. As a consequence, the energy for optical transitions varies with the magnetic field. Since absorption imaging requires closed cycling transitions, it is essential to understand the energy levels of cesium in the high magnetic field regime which refers to field strengths B between 100 G and 1400 G given by our magnetic field system.

This chapter gives an overview of the hyperfine structure and a characterization of ^{133}Cs in external magnetic fields. A brief introduction of the atomic properties of ^{133}Cs is given in Sec. 2.1, followed by a description of ^{133}Cs in the Zeeman- and the Paschen-Back regime. Finally in Sec. 2.3 optical cycling transitions for high-field imaging are presented based on calculations of dipole matrix elements.

2.1 Hyperfine structure of cesium

Cesium is an alkali metal with one electron in the outer shell $n = 6$, occupying the ground state $6^2S_{1/2}$. The excited state has the total angular momentum quantum number $J = 1/2, 3/2$, leading to the characteristic transitions, the D₁-transition $6^2S_{1/2} \leftrightarrow 6^2P_{1/2}$ and D₂-transition $6^2S_{1/2} \leftrightarrow 6^2P_{3/2}$. The coupling $\vec{\mathbf{F}} = \vec{\mathbf{I}} + \vec{\mathbf{J}}$ of the nuclear momentum $\vec{\mathbf{I}}$ with the total angular momentum $\vec{\mathbf{J}}$ leads to the hyperfine structure of the energy levels with the Hamiltonian [33]

$$\hat{H}_{\text{HFS}} = A_{\text{HFS}} \frac{\vec{\mathbf{I}} \cdot \vec{\mathbf{J}}}{\hbar^2} = A_{\text{HFS}} \cdot \frac{(\vec{\mathbf{F}}^2 - \vec{\mathbf{J}}^2 - \vec{\mathbf{I}}^2)}{2\hbar^2}. \quad (2.1)$$

The corresponding hyperfine energy shift is given by [33, 34]

$$\Delta E_{\text{HFS}} = \frac{A_{\text{HFS}}}{2}(F(F+1) - J(J+1) - I(I+1)), \quad (2.2)$$

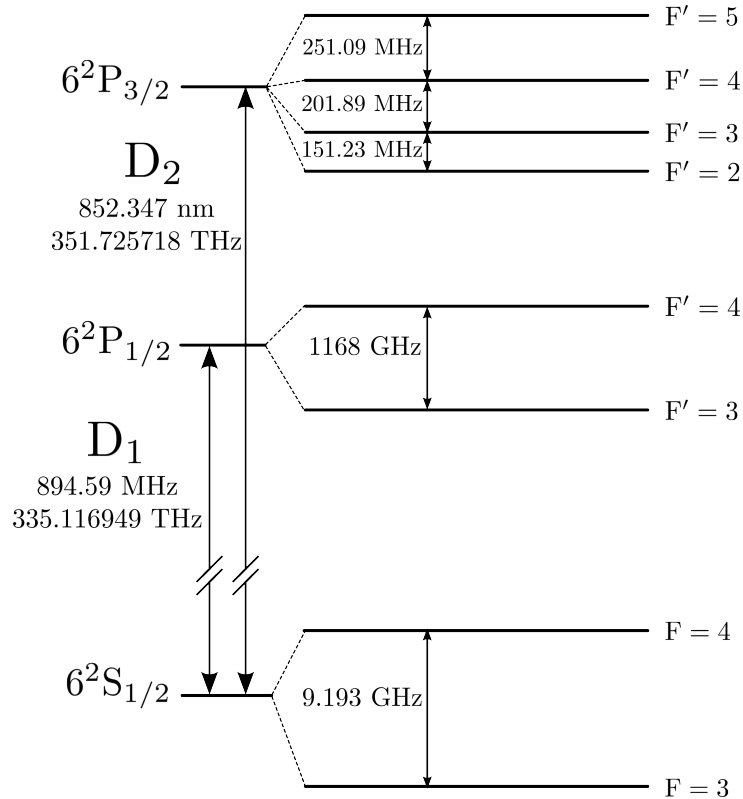


Figure 2.1: Hyperfine structure of cesium. In the experiment the D_2 -transition is used.

where A_{HFS} describes the magnetic dipole constant¹. For absorption imaging closed optical transitions are needed. Since only the D_2 -line fulfills this condition, it is used in the experiment and therefore described only in the following. Fig. 2.1 shows the hyperfine energy structure, where the states are split by the atomic angular momentum quantum number $F = I + J$. The ground state $6^2S_{1/2}$ features a splitting in two hyperfine states $F = 3$ and $F = 4$ with an energy difference of $h \cdot 9.193$ GHz. The excited state $6^2P_{3/2}$, however, shows four different hyperfine states $F' = 2, 3, 4, 5$, with the energy difference $h \cdot 151.23$ MHz ($F' = 2 \leftrightarrow F' = 3$), $h \cdot 201.89$ MHz ($F' = 3 \leftrightarrow F' = 4$) and $h \cdot 251.09$ MHz ($F' = 4 \leftrightarrow F' = 5$). In Appendix A all important quantities and properties of the D_2 -transition are listed. The hyperfine structure is completely described by the basis $|(JI)Fm_F\rangle$, which consists of a set of "good" quantum numbers. However, the basis can change if the atom is perturbed by an external potential as e.g. a magnetic field B .

¹ Definition of the magnetic dipole constant: $A_{\text{HFS}} = \frac{g_I \mu_N B_J}{\sqrt{J(J+1)}}$ [34], with the Landé factor g_I and the magnetic field B_J induced by the precession of the total electron angular momentum.

2.2 Interaction of cesium atoms with an external magnetic field

By applying an external magnetic field the hyperfine energy levels are split into their magnetic sublevels. This can be described by the following Hamiltonian [33]:

$$\hat{H} = \hat{H}_{\text{HFS}} + \hat{H}_{\text{B}} = A_{\text{HFS}} \frac{\vec{\mathbf{I}} \cdot \vec{\mathbf{J}}}{\hbar^2} + \left(g_J \mu_B \frac{\hat{J}_Z}{\hbar} - g_I \mu_N \frac{\hat{I}_Z}{\hbar} \right) \cdot \mathbf{B} \quad (2.3)$$

where H_{B} represents the interaction with the magnetic field $\vec{B} = B \cdot \hat{\mathbf{e}}_z$, that is assumed to be directed in z-direction $\hat{\mathbf{e}}_z$. g_J is the electronic orbital and g_I the nuclear Landé factor, μ_B describes Bohr's magneton and μ_N the nuclear magneton whose values are listed in Tab. A.2. The angular momentum $\vec{\mathbf{J}}$ as well as the nuclear spin $\vec{\mathbf{I}}$ interact with the magnetic field, which results in a splitting of the hyperfine state into their magnetic sublevels with an energy shift ΔE_{B} . Depending on the magnetic field strength the hyperfine coupling between $\vec{\mathbf{J}}$ and $\vec{\mathbf{I}}$ can break up and the splitting of the hyperfine energy levels obeys a different set of good quantum numbers.

Zeeman effect

If the energy shift ΔE_{B} is small compared to the hyperfine interaction ΔE_{HFS} , the atomic states are well described in the basis $|(JI), Fm_F\rangle = |Fm_F\rangle$, which is called Zeeman effect. The interaction Hamiltonian \hat{H}_{B} can be therefore described by

$$\hat{H}_{\text{B},|F,m_F\rangle} = g_F \mu_B \frac{\hat{F}_Z}{\hbar} B , \quad (2.4)$$

with the Landé factor g_F :

$$g_F \approx g_J \frac{F(F+1) - I(I+1) + J(J+1)}{2F(F+1)} . \quad (2.5)$$

For weak magnetic fields the hyperfine states split finally according to

$$\begin{aligned} \Delta E &= \Delta E_{\text{HFS}} + \Delta E_{\text{B},|F,m_F\rangle} \\ &= \frac{A_{\text{HFS}}}{2} (F(F+1) - J(J+1) - I(I+1)) + g_F \mu_B m_F B . \end{aligned} \quad (2.6)$$

Paschen - Back effect

For strong magnetic fields \vec{J} and \vec{I} decouple and the energy levels are described by the quantum numbers m_J and m_I . In this case the magnetic field induced energy shift exceeds the hyperfine regime $\Delta E_B \gg \Delta E_{\text{HFS}}$, which is called the Paschen-back effect. In this regime the system is characterized in the basis $|Jm_JIm_I\rangle$ and the interaction with the magnetic field is described by the Hamiltonian $\hat{H}_{B,|Jm_JIm_I\rangle}$, that is given by Eq. 2.3. The energy shift is therefore given by [33]

$$\begin{aligned}\Delta E &= \Delta E_{\text{HFS}} + \Delta E_{B,|Jm_JIm_I\rangle} \\ &= A_{\text{HFS}} m_J m_I + (g_J \mu_B m_J - g_I \mu_N m_I) B .\end{aligned}\quad (2.7)$$

Both effects, the Zeeman and Paschen-Back effect, represent only the cases for weak and strong magnetic fields. However, for the intermediate case the energy shift ΔE has to be calculated by diagonalizing the total Hamiltonian in Eq. 2.3 at each magnetic field. In Fig. 2.2 the energy splitting of the hyperfine states is shown for the D_2 -transition. The lower figure shows the ground state and the upper picture the excited state manifold, respectively.

The ground - state $6^2S_{1/2}$

For experimental accessible magnetic fields of up to 1400 G, F and m_F are good quantum numbers for the ground state $6^2S_{1/2}$. Thus the splitting is still dominated by the Zeeman effect and follows the energy shift in Eq. 2.6. An exact expression can be given by diagonalizing the Hamiltonian \hat{H}_B in Eq. 2.3. This leads to an analytical expression, which describes the energy splitting for arbitrary magnetic fields. Thus it is valid for the Zeeman- and the Paschen-Back regime. The so-called Breit-Rabi formula [33, 35, 36] is given by

$$\Delta E_{|J=1/2m_JIm_I\rangle} = -\frac{\Delta E_{\text{HFS}}}{2(2I+1)} + g_I \mu_B m B \pm \frac{\Delta E_{\text{HFS}}}{2} \sqrt{1 + \frac{4m}{2I+1} \cdot x + x^2} , \quad (2.8)$$

with $m = m_I \pm m_J = m_I \pm 1/2$ (\pm denotes the same as in Eq. 2.8) and x is defined as

$$x = \frac{(g_J - g_I)\mu_B B}{\Delta E_{\text{HFS}}} . \quad (2.9)$$

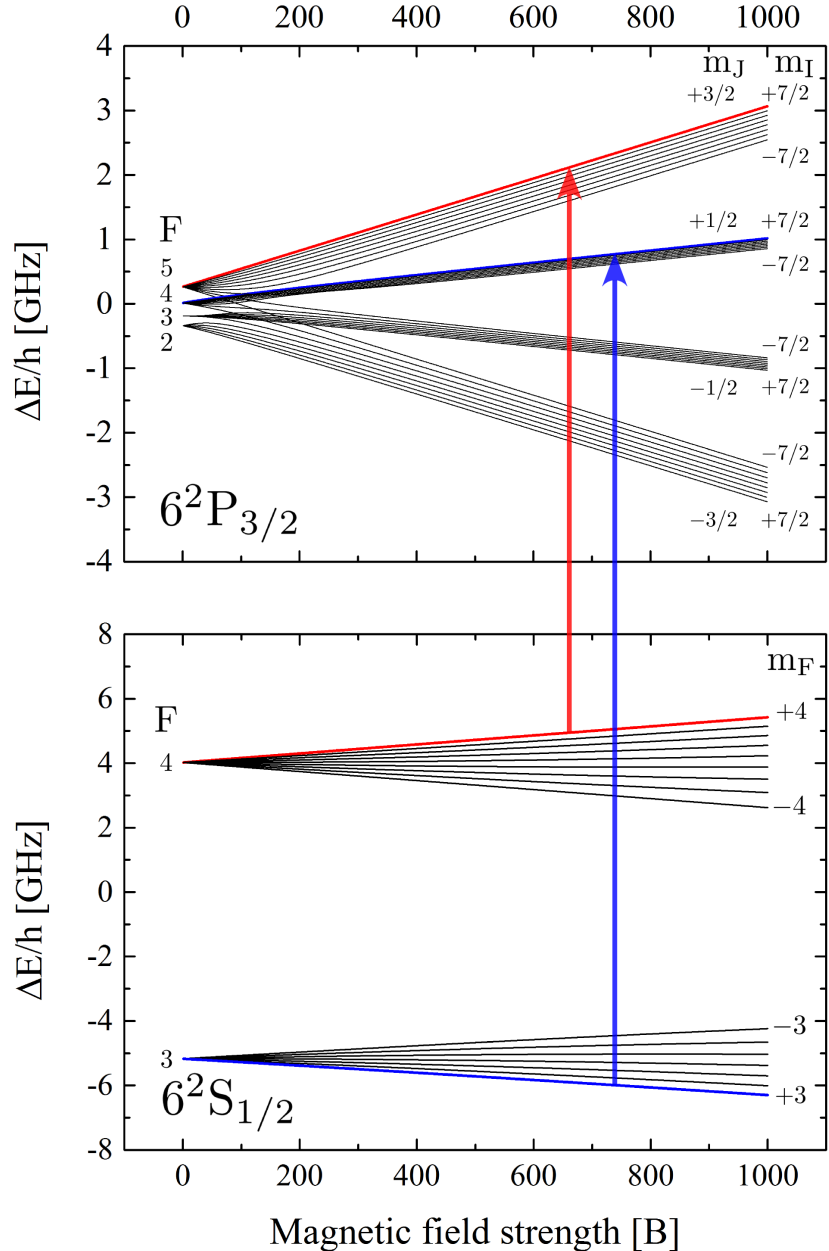


Figure 2.2: Energy splitting of the ground-state $6^2S_{1/2}$ and excited state $6^2P_{3/2}$ in an external magnetic field. The repumping (blue) and imaging (red) transition for high magnetic fields are represented by the arrows and the highlighted energies.

The excited - state $6^2P_{3/2}$

For magnetic fields applied for high-field imaging (100 - 1400 G) the energy splitting of the excited state $6^2P_{3/2}$ is dominated by the Paschen-Back effect, which is due to the small energy differences between the hyperfine states. As a result, the Paschen-Back regime is already reached at ~ 500 G. For lower magnetic field strengths between ~ 60 G and ~ 250 G, however, the excited state is in the intermediate regime. Here, the energy states are shifted, so that they overlap for certain magnetic fields. This means, for an increasing magnetic field, from weak to strong magnetic fields, crossings between states with different $m_F = m_I + m_J$ occur. In order to consider these state mixing effects, the interaction Hamiltonian \hat{H}_B has to be diagonalized at every magnetic field. In this thesis the energy states have been calculated by transforming the Hamiltonian $\hat{H}_B = \hat{H}_{B,|Jm_JIm_I\rangle}$, which is diagonal in the Paschen-Back regime, into the low-field or Zeeman regime, respectively, with basis $|(JI)Fm_F\rangle$:

$$\begin{aligned}\Delta E_B &= \langle (JI)Fm_F | \hat{H}_B | (JI)Fm_F \rangle \\ &= U^{-1} \cdot \langle Jm_JIm_I | \hat{H}_B | Jm_JIm_I \rangle \cdot U.\end{aligned}\tag{2.10}$$

U is the transformation matrix whose matrix elements are described by *Clebsch-Gordon coefficients* (CGC) (the definition of CGC is given in Eq. 2.17):

$$U_{m_F, m_I m_J} = \langle (JI)Fm_F | Jm_JIm_I \rangle .\tag{2.11}$$

With the detailed knowledge about the energy structure of Cs at arbitrary magnetic field strengths, suitable optical cycling transitions can be obtained for the high-field imaging.

2.3 Optical cycling transitions

At zero magnetic field Cs atoms are imaged by the closed transition $F = 4 \rightarrow F' = 5$. But since most of the experiments are done in the ground state $|F = 3, m_F = 3\rangle$, an additional laser is used to pump atoms into $F' = 4$, from where they decay into $F = 4$. Since a decay from $F' = 4$ into $F = 3$ is also allowed, this happens with a small leakage rate ($\sim 9.7\%$). Imaging at high magnetic fields, however, needs a detailed analysis of allowed optical cycling transitions, because ground and excited state of the D_2 -transition split by different sets of good quantum numbers, as described in the previous Sec. 2.2. For this purpose transition dipole matrix elements are determined.

Dipole matrix elements

The here presented concept for determination of the dipole matrix elements follows same calculations in the PhD thesis of Martin Berninger [37] and similar in textbooks [38].

According to Fermi's Golden Rule the probability for a transition² $|g\rangle \rightarrow |e\rangle$ is proportional to the absolute square of the dipole matrix element d :

$$W_{ge} \propto |d|^2 . \quad (2.12)$$

Therefore the transition strength can be well estimated by obtaining the dipole matrix element, which is defined by:

$$d = \langle g | \vec{d} \cdot \vec{\epsilon} | e \rangle , \quad (2.13)$$

where $\vec{d} = -e\vec{r}$ describes the dipole moment operator and $\vec{\epsilon}$ the polarization vector of the incident light field. The product $\vec{d} \cdot \vec{\epsilon}$ can be expressed in spherical coordinates:

$$\vec{d} \cdot \vec{\epsilon} = \sum_{q=-1}^{+1} d_q \epsilon_q , \quad (2.14)$$

with ϵ_q in basis of σ^\pm - and π -light:

$$\underbrace{\epsilon_{\pm 1} = 1/\sqrt{2}(e_x \pm ie_y)}_{\sigma^\pm-\text{light}}, \underbrace{\epsilon_0 = e_z}_{\pi-\text{light}} . \quad (2.15)$$

Since the ground state $6^2S_{1/2}$ is split by the Zeeman effect and the excited state $6^2P_{3/2}$ by the Paschen-Back effect (see Sec. 2.2), the dipole moment is expressed in the basis

$$|g\rangle = |(JI)Fm_F\rangle , |e\rangle = |J'm'_J I'm'_I\rangle ,$$

and is given by

$$d = \sum_{q=-1}^{+1} \langle (JI)Fm_F | d_q \epsilon_q | J'm'_J I'm'_I \rangle . \quad (2.16)$$

This expression can be simplified by using the definition of *Clebsch-Gordon coefficients* (CGC) [38]:

$$|(JI)Fm_F\rangle = \sum_{m_J=-J}^J \sum_{m_I=-I}^I \underbrace{\langle Jm_J Im_I | (JI)Fm_F \rangle}_{\text{Clebsch-Gordon-Coefficient}} |Jm_J Im_I \rangle . \quad (2.17)$$

² $|g\rangle$ stands for the ground state and $|e\rangle$ for the excited state

2 Cesium at high magnetic fields

For a better representation the CGC are expressed in terms of *Wigner 3j-symbols*:

$$\langle Jm_J Im_I | (JI)Fm_F \rangle = (-1)^{I-J-m_F} \sqrt{2F+1} \begin{pmatrix} J & I & F \\ m_J & m_I & -m_F \end{pmatrix}. \quad (2.18)$$

Due to the fact that the incident light field does not interact with the nuclear spin, transitions can be constrained to $I = I'$ and $m_I = m'_I$ [37]. This leads to the dipole matrix element:

$$d = \sum_{q=-1}^{+1} \sum_{m_J=-J}^J (-1)^{I-J-m_F} \sqrt{2F+1} \begin{pmatrix} J & I & F \\ m_J & m_I & -m_F \end{pmatrix} \cdot \langle Jm_J | d_q | J'm'_J \rangle \cdot \epsilon_q. \quad (2.19)$$

The dipole matrix can be further reduced to only one particular quantum number by using the *Wigner-Eckart theorem* [38], with which the dipole operator is expressed as the product of CGC and the *reduced matrix* $\langle J || d_q || J' \rangle$ [37]:

$$\begin{aligned} \langle Jm_J | d_q | J'm'_J \rangle &= \langle J'm'_J 1q | Jm_J \rangle \frac{\langle J || d_q || J' \rangle}{\sqrt{2J'+1}} \\ &= (-1)^{1-J'-m_J} \sqrt{2J+1} \begin{pmatrix} J' & 1 & J \\ m'_J & q & -m_J \end{pmatrix} \cdot \frac{\langle J || d_q || J' \rangle}{\sqrt{2J'+1}}. \end{aligned} \quad (2.20)$$

The dipole matrix element for transitions in Cs at high magnetic fields is finally given by

$$\begin{aligned} d &= \sum_{q=-1}^{+1} \sum_{m_J=-J}^J (-1)^{I-J-m_F+1-J'-m_J} \sqrt{2F+1} \frac{\sqrt{2J+1}}{\sqrt{2J'+1}} \cdot \\ &\quad \begin{pmatrix} J & I & F \\ m_J & m_I & -m_F \end{pmatrix} \begin{pmatrix} J' & 1 & J \\ m'_J & q & -m_J \end{pmatrix} \cdot \langle J || d_q || J' \rangle \cdot \epsilon_q. \end{aligned} \quad (2.21)$$

A full calculation of d is not necessary, since one is only interested in the relative transition strength. Thus, it is sufficient to determine and compare the following factors S_{rel} , which provides a measure of the relative strength of each transition $|Fm_F\rangle \leftrightarrow |m_Jm_I\rangle$ [37]:

$$|d_q|^2 \propto S_{q, |F, m_F\rangle \leftrightarrow |m_I, m_J\rangle}^{\text{rel}} = (2F+1) \left| \begin{pmatrix} J & I & F \\ m_J & m_I & -m_F \end{pmatrix} \begin{pmatrix} J' & 1 & J \\ m_J & q & -m'_J \end{pmatrix} \right|^2. \quad (2.22)$$

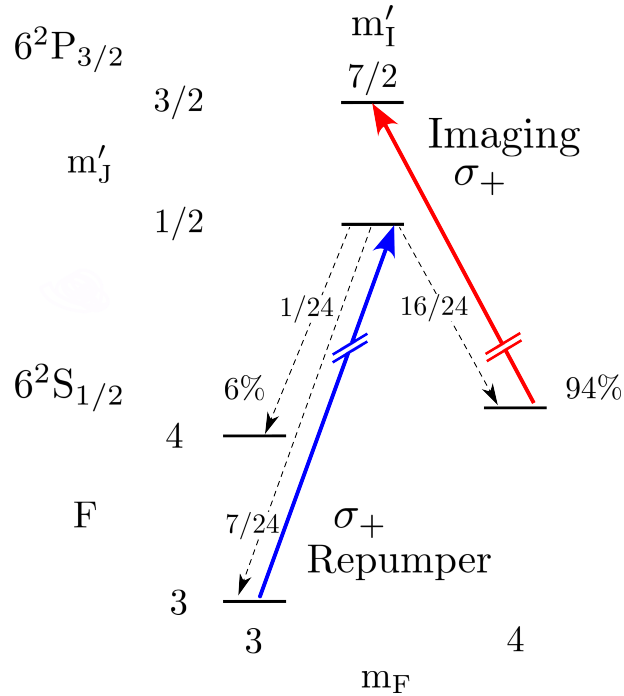


Figure 2.3: Repumper (blue) and imaging (red) transition for high magnetic fields used in the experiment. The solid lines represent the transitions with a σ_+ -polarization, whereas the dashed lines represent possible decay channels from $|m_I = 7/2, m_J = 1/2\rangle$. Their relative transition strengths (see text) is described by the numbers. $\sim 6\%$ of the atoms are end up in the dark state $|F = 4, m_F = 3\rangle$. The figure was adapted from [37].

Imaging transition

As for zero magnetic field ($F = 4 \rightarrow F' = 5$), imaging at high fields is performed from the state³ $F = 4$. Therefore two closed transitions $|F = 4, m_F = \pm 4\rangle \rightarrow |m'_I = \pm 7/2, m'_J = \pm 3/2\rangle$ can be used. But since we are using σ^+ -light for imaging, the transition $|F = 4, m_F = +4\rangle \rightarrow |m'_I = +7/2, m'_J = +3/2\rangle$ is implemented in the experiment. From the calculations of the energy structure in Sec. 2.2, one can obtain the transition frequency and its shift for an arbitrary magnetic field. The imaging transition is detuned by 1.40 MHz/G in an external magnetic field related to the hyperfine transition at zero-magnetic field $F = 4 \rightarrow F' = 5$ (see Fig. 2.4).

³ In principle imaging from $F = 3$ is also possible, but it is significantly influenced by a strong leakage rate into the state $F = 4$.

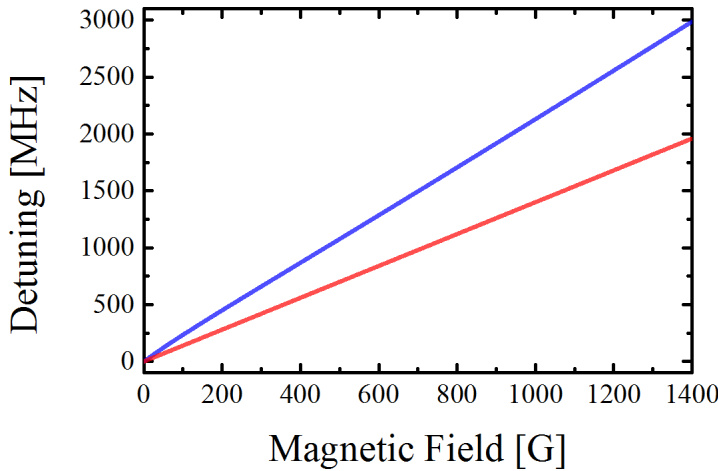


Figure 2.4: Detuning of the repumper (blue) $|F = 3, m_F = 3\rangle \rightarrow |m'_J = 1/2, m'_I = 7/2\rangle$ and imaging (red) transition $|F = 4, m_F = 4\rangle \rightarrow |m'_J = 3/2, m'_I = 7/2\rangle$ for an applied magnetic field. The repumper transition is detuned by 2.12 MHz/G and the imaging transition by 1.40 MHz/G.

Repumping transition

In contrast to imaging the choice of an appropriate repumping transition needs a detailed analysis. This is due to a number of available transitions from the ground state $F = 3$ in high magnetic fields (see Fig. 2.2). However, this analysis can be restricted. The atoms have to be pumped into the state $|F = 4, m_F = 4\rangle$, which is related to the $m_I = 7/2$ and $m_J = 1/2$. This means that atoms have to be excited into an intermediate state, from which a decay into $|F = 4, m_F = 4\rangle$ is allowed. Since the selection rules $\Delta m_I = 0$, $\Delta m_J = 0, \pm 1$ have to be fulfilled, two transitions are available [37]:

$$\begin{aligned} |1\rangle &: |F = 3, m_F = 3\rangle \rightarrow |m'_I = 7/2, m'_J = 1/2\rangle \\ |2\rangle &: |F = 3, m_F = 3\rangle \rightarrow |m'_I = 7/2, m'_J = -1/2\rangle \end{aligned}$$

The calculations of the relative transition strength S^{rel} (see Eq. 2.22) show that transition $|1\rangle$ is stronger (see Tab. A.3 in Appendix A), for which reason this one is used in the experiment. But, this repumping transition is not ideal, because of a feasible decay into $|F = 4, m_F = 3\rangle$. This corresponds to a leakage rate⁴ of 6.25%, which has to be considered in the calculation of the absorption cross section (see Sec. 4.1). An overview of both transitions is given in Fig. 2.3 as well as in Fig. 2.2.

⁴ The leakage rate is determined by comparing the factor S^{rel} of both transitions: $S_{|3,4\rangle \leftrightarrow |7/2,1/2\rangle}^{\text{rel}} / S_{|4,4\rangle \leftrightarrow |7/2,1/2\rangle}^{\text{rel}} = 0.0625$

In an external magnetic field the repumper transition $|F = 3, m_F = 3\rangle \rightarrow |m_I = 7/2, m_J = 1/2\rangle$ is detuned by 2.12 MHz/G, which is larger as for the imaging transition with 1.40 MHz/G as shown in Fig. 2.4. The experimentally accessible magnetic fields of up to 1400 G, leads therefore to a frequency shift of ~ 3000 MHz and ~ 2000 MHz. In order to image atoms at these magnetic field strengths, the laser frequencies have to be detuned by the same frequency values.

3. High-field imaging system

The detection of cesium atoms in an external magnetic field was not possible with the previous low-field imaging, since the laser frequency could not be changed by the same value as the frequency shift of the imaging transition (see Ch. 2). Therefore, an additional setup, the high-field imaging system, was assembled, which enables imaging of cesium atoms at magnetic field strengths up to which the experiment is designed. In this chapter the implementation of the high-field imaging setup is described. A characterization of the laser system, as well as of the optical setup and the locking scheme is given in the first part Sec. 3.1. The second part Sec. 3.2 specifies and characterizes the laser frequency stabilization.

3.1 Laser system

The main laser system of the LiCs-experiment consists of two extended-cavity diode lasers (ECDL), which are used as the light source for different cooling and trapping steps, for example Zeeman cooling, the magneto-optical trap (MOT) and further cooling steps. For simplicity, the lasers are called *master cooler* (TOPTICA TA PRO 850), the laser that is used for the cooling, and *master repumper* (TOPTICA DL PRO 850), the laser that is used for repumping. The *master cooler* is further used also for imaging at zero or low magnetic fields, whereby the closed transition $F = 4 \rightarrow F' = 5$ is detected as discussed in the previous section. But, since the atoms are prepared in the ground state $F = 3$, the *master repumper* is needed, which pumps atoms into $F = 3 \rightarrow F' = 4$, from which they decay into $F = 4$, where atoms can be imaged. A detailed description about the laser system and the low-field imaging setup is given in previous theses by Stefan Schmidt [39] and Marc Repp [40].

The required detuning of the laser frequency by several GHz for high field imaging cannot be provided by the frequency lock of the ECDLs stated above. Therefore, two additional lasers, the high-field imaging lasers, are needed, one for repumping and the

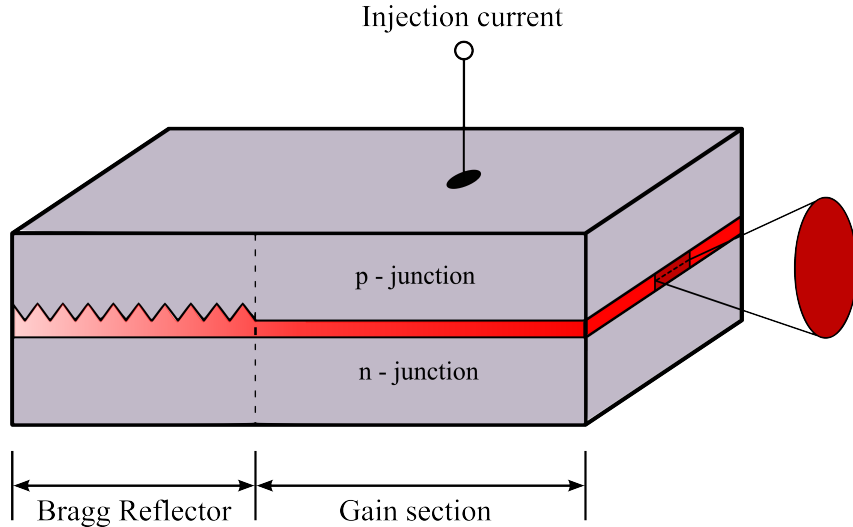


Figure 3.1: Schematic setup of a Distributed Bragg Reflector (DBR) laser diode. The grating (so-called Bragg reflector), is located aside the gain section.

other for imaging atoms. Both are stabilized by *frequency offset locking*, which describes a technique to stabilize a laser, the slave, to a reference laser, the master, with a certain frequency offset. In our case the imaging laser for high fields is locked on the *master cooler* and the high-field repumper laser on the *master repumper*. For this purpose, light, provided by both the slave and the master laser, is superimposed and the ensuing beat signal is detected by a photodiode. The frequency of the beat-note is then mixed with a frequency provided by a voltage-controlled oscillator (VCO). By tuning the VCO the slave laser's frequency can be thus controlled and adjusted to reach the imaging transition. A detailed explanation as well as the experimental implementation based on the scheme, that is presented in reference [28], is given in Sec. 3.2. The lasers, that are used for high-field imaging, are DBR lasers, which are explained in more detail below.

3.1.1 DBR laser

Common wavelength selective lasers are e.g. extended cavity diode laser (ECDL)[41] or distributed Bragg reflector (DBR) lasers [42]. Both laser types are based on the working principle of a semiconductor laser diode. In a p-n-junction diode a population inversion is created. By applying a forward bias voltage, carrier pairs are injected into the junction region and recombined by means of stimulated emission [43]. This emitted light can inject carrier pairs again by the photo-electrical effect and consequently amplifies the output. At the edges of the laser diode the refractive index changes by means of a varying charge carrier density, whereby an internal cavity is created. Since the bandwidth of

the laser diode is typically on the order of a few THz, many internal modes (induced by the internal cavity) survive the mode competition. In order to enable a single mode and simultaneously a wavelength selective operation the laser diode has to be extended by a grating [44] inside or outside the laser diode. In this way an additional cavity is created, whose modes are narrower as the internal ones. The ECDL for example has an external grating [41] providing a typical laser linewidth of few ~ 100 kHz, whereas in DBR lasers¹ an internal grating is used, which is formed by a periodic corrugation aside the gain medium [42] as illustrated in Fig. 3.1. It consists of a (dielectric) medium with a lateral periodic structure with varying refractive index. The grating period is chosen as half of the desired wavelength leading to a constructive interference of the reflected beams and thus to a large net reflection. The laser linewidth is generally on the order of few MHz, but compared to other laser types, the biggest advantage of a DBR laser is the large continuous frequency tuning range of typically 50 GHz [45] for modern lasers. This makes this type of laser ideal for the application of high-field imaging as presented in this thesis.

Characterization of the used DBR lasers

In our setup home-built DBR lasers are used (laser diode: SDL-5712-H by Spectra Diode Lasers Inc.). They are stabilized at room temperature and their output is regulated by an applied injection current. Besides the lasers, the controllers are also home-built. The diodes emit at 852 nm and have a maximal power of $P_{\max} = 100$ mW. The lasing threshold is estimated by $I_{\text{th}} = 27.4$ mA for the repumper and $I_{\text{th}} = 22.7$ mA for the imaging laser. The laser frequency is shifted by changing the injection current, which varies the refractive index and therefore the internal cavity. The laser linewidths could be estimated to ~ 6.2 MHz for the imaging and ~ 14.1 MHz for the repumper laser, as it will be described in Sec. 3.2.3. Since both lasers are home-built, it is likely that the discrepancy between both values results from small differences in the installation as for example in the individual electronic setup.

Since the laser frequency has to be tuned by few GHz, the tuning ranges of the DBR lasers have been investigated. While tuning the injection current, a wavemeter (HIGH FINESSE, ÅNGSTROM WS/7, absolute accuracy: 60 MHz, relative accuracy: 10^{-7}) measures the absolute laser frequency as depicted in Fig. 3.2. The spectrum shows different frequency hops. This is due to competition of the internal modes, where only the mode is

¹ A similar laser type is the Distributed Feedback (DFB) laser, which have an internal grating inside the gain medium. This provides similar features as for the DBR laser.

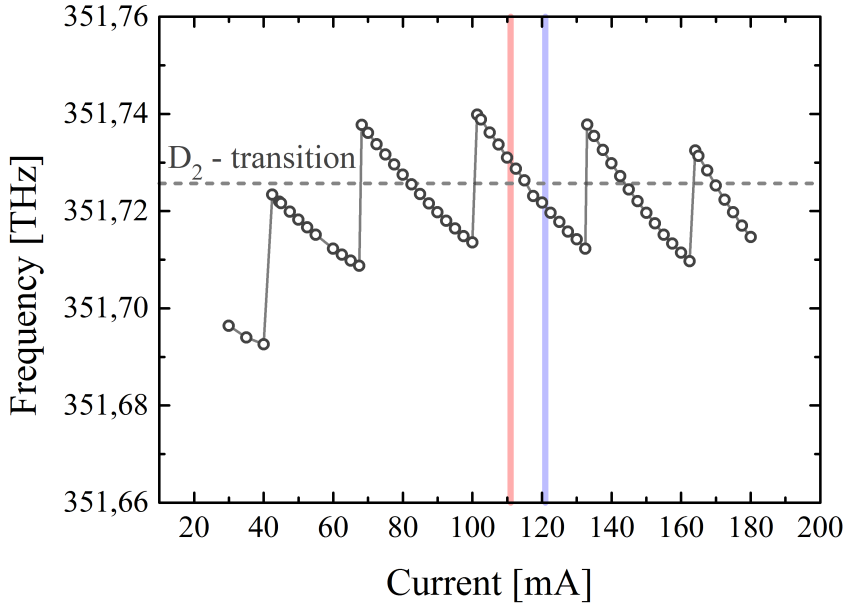


Figure 3.2: Frequency of the HFI lasers vs. injection current. The spectrum shows a number of mode-hop free ranges. Between ~ 60 and ~ 160 mA, a frequency tuning of ~ 27 GHz over 30 mA is possible. In the experiment the indicated mode around 120 mA is chosen. The laser diode's temperature is adjusted so that the D_2 -transition lies in the center of the mode. The red and blue vertical lines show the working region for the repumper (blue) and imaging laser (red).

emitted that fulfills the gain condition. The measured mode-hop free ranges (around the D_2 -transition) have a size of ~ 27 GHz (corresponding to 0.07 nm) over ~ 30 mA, which ensures a sufficiently wide tuning range for high-field imaging.

3.1.2 Locking Scheme

Since the HFI lasers are stabilized on the *master repumper* and *master cooler*, the locking scheme and also the optical setup has to be adapted to the existing laser system. Both master lasers are used as main light sources for cooling and trapping light in the experiment. For this purpose both are stabilized on atomic transitions via spectroscopy, from which the required frequencies are shifted by acoustic-optical modulator (AOM). The *master cooler* is locked on the transition $F = 4 \rightarrow F' = 3$ via modulation transfer spectroscopy (MTS) [46], from where the imaging light is shifted by +450 MHz, ensuring $F = 4 \rightarrow F' = 5$ for the low-field imaging setup as illustrated schematically in Fig. 3.3. The *master repumper*, however, is stabilized on the crossover $F = 3 \rightarrow X_{34}$ via frequency modulation spectroscopy. The crossover is used because of practical reasons.

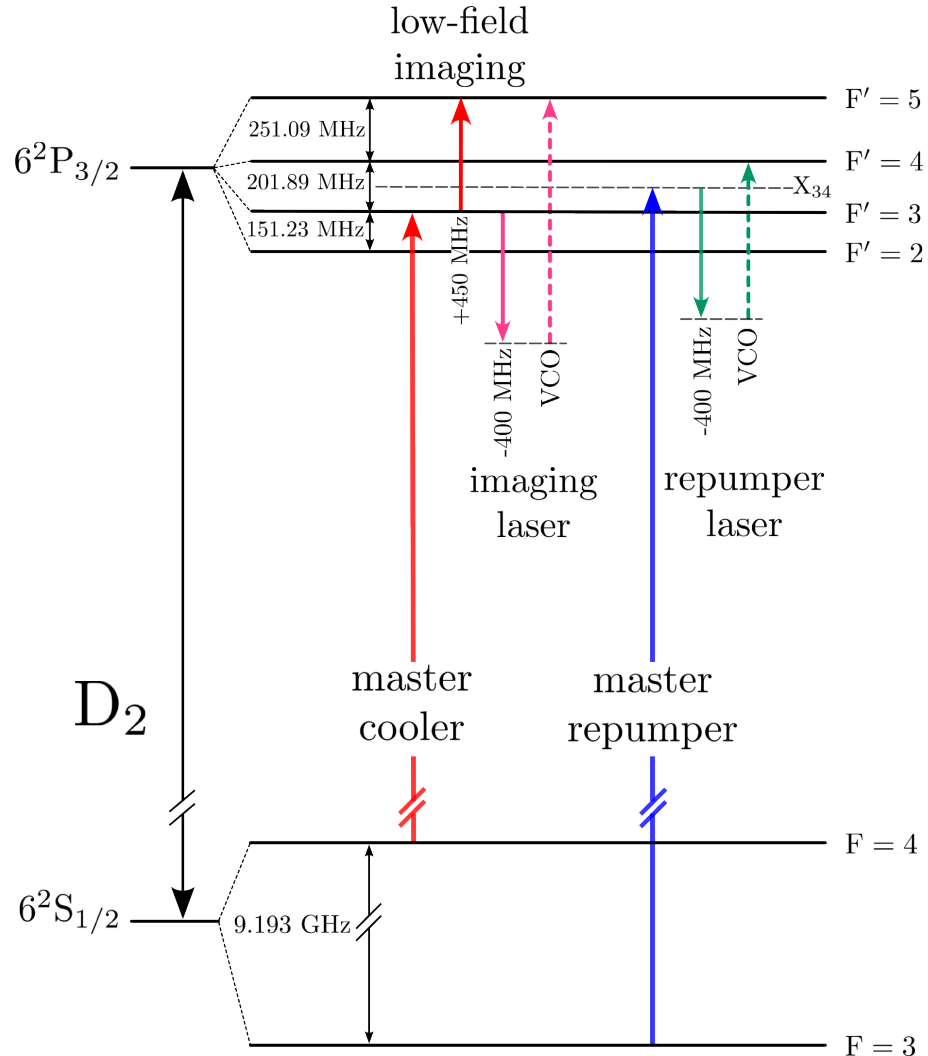


Figure 3.3: Locking scheme for HFI lasers. The figure shows the locking scheme for the case of imaging at zero field with both, the low-field and the high-field imaging system. The *master cooler* are locked on the transition $F = 4 \rightarrow F' = 3$ and the *master repumper* on $F = 3 \rightarrow X_{34}$. Low-field imaging is enabled by shifting light that is provided by the *master cooler* by $+450$ MHz, so that the atoms can be imaged by the transition $F = 4 \rightarrow F' = 5$. The HFI lasers (purple and green) are locked to the master laser (red and blue) and first shifted down by -400 MHz with an AOM and with VCOs up to reach the required transition. For imaging at zero magnetic fields, the VCO is detuned by $+850$ MHz for the imaging laser and by $+500$ MHz for the repumper (dashed arrows), whereas at high magnetic fields the VCO frequencies are shifted to larger values, so that the HFI lasers are resonant to the high-field imaging and repumping transitions.

The HFI laser frequencies are offset locked to the master lasers and shifted by a VCO to reach the required state. The laser light is first detuned by -400 MHz with an AOM in double-pass configuration and shifted by +850 MHz for the imaging laser and +500 MHz for the repumper laser to the corresponding transitions for zero-field imaging.

If a magnetic field is applied the VCO frequencies are detuned to larger values, so that the HFI lasers are resonant to $|F = 3, m_F = 3\rangle \rightarrow |m'_I = 7/2, m'_J = 1/2\rangle$ for repumping and $|F = 4, m_F = 4\rangle \rightarrow |m'_I = 7/2, m'_J = 3/2\rangle$ for imaging, respectively (see Fig. 2.3).

3.1.3 Optical setup

The optical setup for high-field imaging consists basically of two parts as depicted in Fig. 3.4: a setup for preparing the imaging light (red box) and a setup for generating a beat signal between slave and master laser for frequency stabilization (green box). The illustrated optical setup in Fig. 3.4 gives a simplified schematic overview for one laser, since the setup for both HFI lasers are similar. A detailed figure of the setup is given in the appendix D. The HFI lasers are set to an injection current of ~ 120 mA for the repumper and ~ 111 mA for the imaging laser, providing ~ 70 mW and ~ 65 mW for the optical setup, respectively.

The output beam of the HFI laser is guided through an optical isolator (ISOWAVE, I-80-U4, -60dB attenuation), which is used to protect the laser diode from back reflections by subsequent optical elements. Since the elliptical output beam is larger than the isolator's aperture (2 mm), a prism pair is placed in front of the isolator. An optical power of ~ 40 mW is provided behind the isolator for both HFI laser. The first polarizing beam splitter (PBS) PBS1 behind the isolator splits the beam into two parts. The reflected light is used for the high-field imaging itself (red box), whereas the transmitted light is superimposed with the master laser (green box).

In order to obtain as much light as possible for imaging, the $\lambda/2$ -waveplate before PBS1 is adjusted so that $\sim 90\%$ of the light is reflected, which corresponds to about ~ 35 mW for each laser. The reflected beam passes a further beam splitter PBS2, which cleans the polarization of the light so that a well polarized beam is provided for the subsequent AOM. The beam passes the AOM (CRYSTAL TECHNOLOGIES INC., AOM 3200-125, 200 MHz) in double-pass configuration [47] (transmission efficiency: 65 %), whereby the light is shifted by -400 MHz. In order to suppress thermal lensing effects the RF-power of the modulator is maintained to a small value. The AOM is used for frequency scanning, because the double-pass configuration is insensitive to position changes of the back reflected beam when scanning the AOM frequency. Furthermore, the AOM enables a

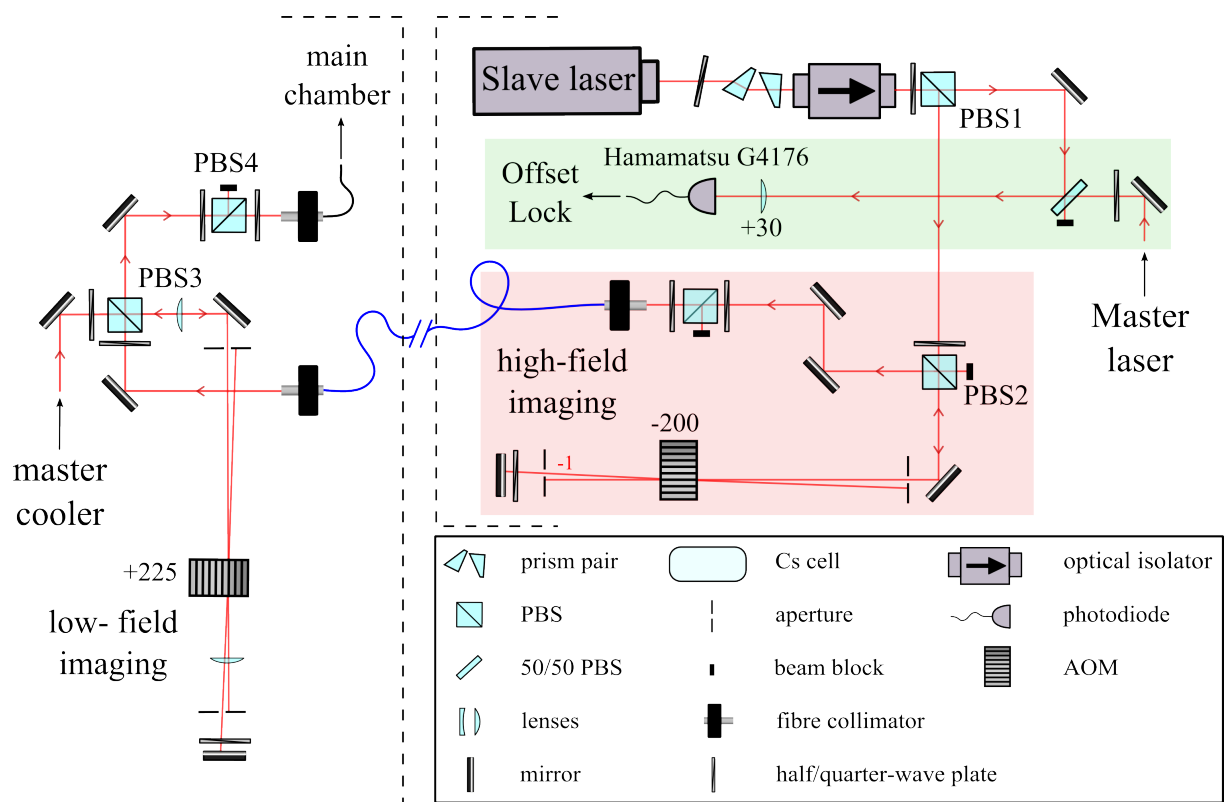


Figure 3.4: Schematic overview of the optical setup. Only the principal setup for one laser is presented, since the setup for both HFI lasers are similar. The high-field setup consists of a part for preparing the imaging light (red box) and a setup for generating a beat signal with the corresponding master laser (green box).

switching and a varying of the imaging and repumper light pulses. After passing the AOM in double-pass configuration the beam is reflected by PBS2 and coupled into a polarization maintaining single-mode fiber (THORLABS, P5-780PM-FC-5, NA=0.12). Well polarized output beams are reached with a power up to ~ 3.2 mW for the imaging and ~ 5.0 mW for the repumping light, respectively. Afterwards the fiber output is overlapped with the low-field imaging light of the main setup at PBS3. Due to the difference of 90° in polarization of low- and high-field light, it is possible to choose between both imaging setups only by changing the $\lambda/2$ -waveplate in front of PBS4. By coupling into the MOT cubes (3D-MOT FIBER PORT CLUSTER, SCHÄFTER & KIRCHHOFF) [39], the imaging light is sent to a side view-port of the main chamber, so that atoms are observed in horizontal plane. Finally, a maximal power of ~ 1.3 mW for the imaging and ~ 2.4 mW for the repumping are available, respectively. With a beam size of about 19.5 mm, this results in an intensity of 0.63 mW/cm², which is below the saturation intensity of 1.1 mW/cm² [36]. But for experiments the imaging power is reduced so that power broadening effects do not occur.

For frequency offset locking the transmitted light at PBS1 is overlapped with the master laser by a non-polarizing 50:50 beam splitter. The resulting beat-note is detected on a fast photodiode (Hamamatsu G4176). To ensure a good beat-signal the intensity of each beam is adjusted to the same value of 1 mW (maximal input power of the photodiode is 5 mW) and their polarizations are matched by varying the $\lambda/2$ -waveplate behind the fiber outcoupler of the master laser. The beat signal is amplified and used to stabilize the slave on the master laser. For this purpose frequency offset locking is implemented, which is explained in the next section.

3.2 Frequency offset locking

In the following the basic concept of frequency offset locking and its experimental implementation as well as a stability and noise analysis is presented.

3.2.1 Principle of offset locking

The basic principle of frequency offset locking is the stabilization of a slave on a master laser with a certain frequency offset. Therefore the beat-note between both is compared with a reference frequency, the local oscillator. An error signal proportional to the difference frequency between beat signal and local oscillator is created and transformed into a DC signal so that the slave laser's frequency can be regulated by a servo loop. Our setup

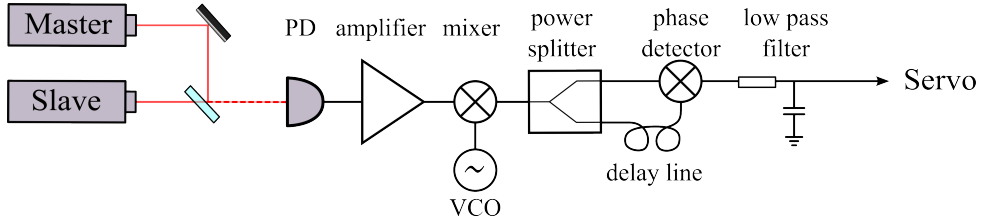


Figure 3.5: Schematic of an offset beat lock setup.

(see Fig. 3.7) follows reference [28], which represents a simple scheme for tunable offset locking up to a few GHz, but there are also similar techniques presented in references [29] and [30].

In Fig. 3.5 a schematic setup is shown. By superimposing the laser beams a beat-note is generated on a photodiode, whose output signal is proportional to the intensity of the incident light:

$$\begin{aligned} I &\propto |E_s \cos(\omega_s t) + E_m \cos(\omega_m t)|^2 \\ &= E_s^2 \cos^2(\omega_s t) + E_m^2 \cos^2(\omega_m t) + 2E_s E_m \cos(\omega_s t) \cos(\omega_m t) , \end{aligned} \quad (3.1)$$

where E_s and E_m describe the electric field amplitudes of both light waves with the frequencies ω_s and ω_m . The index "s" stands for the slave and "m" for the master laser, respectively. With the help of the angle addition theorem the last term in Eq. 3.1 can be simplified to:

$$I \propto E_m E_s \cdot [\cos((\omega_m - \omega_s) \cdot t) + \cos((\omega_m + \omega_s) \cdot t)] , \quad (3.2)$$

where $\Delta\omega = (\omega_m - \omega_s)$ describes the low-frequent and $(\omega_m + \omega_s)$ the high-frequent part, which corresponds to approximately twice the optical frequency of ~ 700 THz. This frequency is larger than the bandwidth of the photodiode and hence not observable. The final output signal consists therefore only of a the low frequency term and a constant offset proportional to the sum of both beam intensities, which can be canceled by coupling the photodiode capacitively (see Fig. 3.7).

In order to lock the laser on a desired offset a stable reference frequency is provided by a voltage controlled oscillator (VCO) with frequency ω_{VCO} . Its output is multiplied with the difference signal by a frequency mixer resulting in an oscillating signal with two frequency components $\omega_{\pm} = \Delta\omega \pm \omega_{\text{VCO}}$:

$$\cos(\Delta\omega t) \cdot \cos(\omega_{\text{VCO}} t) = \frac{1}{2} (\cos((\Delta\omega - \omega_{\text{VCO}})t) + \cos((\Delta\omega + \omega_{\text{VCO}})t)) . \quad (3.3)$$

Since the signal at ω_+ is not needed for generating the error signal and could influence

3 High-field imaging system

the stability, it is convenient to use a low-pass filter with a certain cut-off frequency ω_c in the range $\omega_- < \omega_c < \omega_+$. In this way frequencies above ω_c can be suppressed.

For laser stabilization now an error signal proportional to ω_- has to be created and transformed into a DC signal for the feedback loop. This is done by splitting the signal at ω_- in two equal parts and recombine them on a phase detector while one signal passes an additional delay line. For the delay line a simple coaxial cable is used, which introduces a time delay τ ($\tau \approx 5$ ns for a 1 m cable), which leads to a phase shift $\varphi = \tau \cdot \omega_-$. The resulting output signal is described by

$$S \propto \cos(\omega_- t) \cdot \cos(\omega_- t + \varphi) = \frac{1}{2}(\cos(\varphi) + \cos(2\omega_- t + \varphi)) , \quad (3.4)$$

which consists of a DC part $\cos(\varphi)$, that is only proportional to the phase shift, and an oscillating part, which is filtered out by a subsequent low-pass filter. The error signals is given by

$$S \propto \cos(\varphi) = \cos(\tau \cdot ((\omega_m - \omega_s) - \omega_{VCO})) \quad (3.5)$$

By scanning the frequency of the slave laser, an error signal is obtained that describes a cosine, which is convolved with the bandwidth of the low-pass filter. This leads to the characteristic shape of the output signal depicted in Fig. 3.6 (a). If the slave laser is scanned over the master laser's frequency ω_m two signals can appear, one for the case $\omega_s < \omega_m$ and one for $\omega_s > \omega_m$, while both signals correspond to the same offset frequency

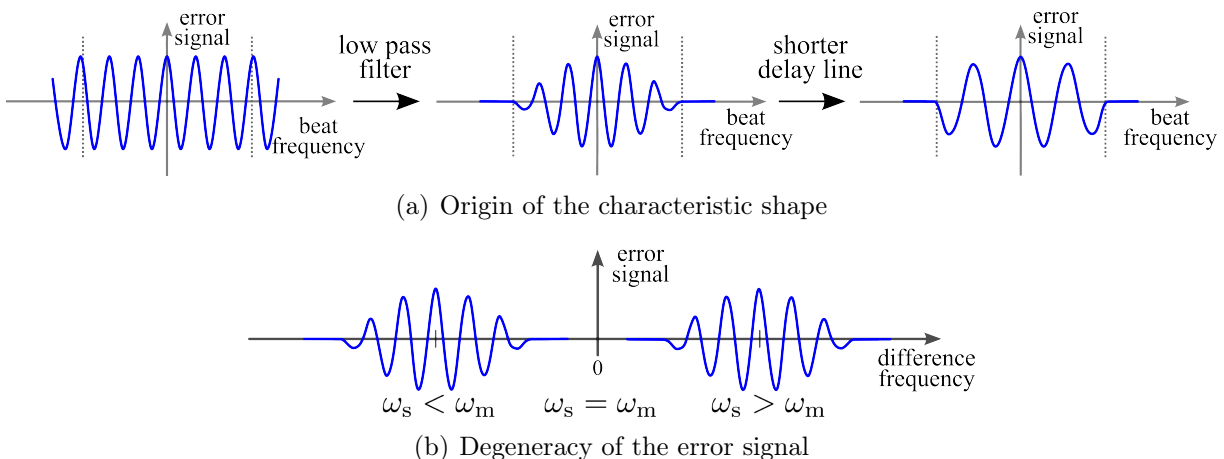


Figure 3.6: Principle of the error signal. (a) The characteristic shape of the error signal is generated by the low pass filter, whereas the number of locking points and thus the slope is dependent on the length of the delay line and hence the induced time delay, respectively. (b) Due to the fact that the slave laser is scanned over the resonance $\omega_m = \omega_s$ two error signals are generated.

ω_{VCO} , as illustrated schematically in Fig. 3.6 (b) and confirmed by experimental results in Fig. 3.8 and 3.9. Since the resulting output signal has many zero-crossings, it can be used as an error signal with different locking points separated by $2\pi/\tau$. The spacing can be varied by changing the length l (in cm) of the delay line, since $\tau \propto l$. This means a smaller delay line would reduce the number of possible locking points and the slope at the zero-crossing, either (see Fig. 3.6). A small change in the beat frequency would thus effect a large change of the error signal. But on the other hand, a small delay line yields to a broader capture range given by $\pm 2\pi \cdot 1/2\tau$ starting from the locking point. The size of the capture range defines the maximal deviation from the set point that is given to the feedback loop (see Sec. 3.2.3). The lock becomes unstable or the signal jumps to the next locking point, if the deviation exceeds the capture range. Therefore the choice of the cable length should be adapted to the certain experimental application.

3.2.2 Setup for offset locking

The implemented frequency offset lock setup follows the principal described in the previous section. It is extended and adapted to experimental requirements. A schematic overview of the offset lock setup is given in Fig. 3.7, where also the used RF-components (MINI-CIRCUITS) are specified.

The beat signal is detected by a fast photodiode (Hamamatsu G4176; $t_{\text{rise}} \simeq t_{\text{fall}} = 30 \text{ ps}$). It is biased by a conventional 9 V battery over a bias tee², with which the DC-part of the beat signal is capacitively filtered out. After filtering, the RF signal is mixed with the local oscillator (LO) by a frequency mixer, whose bandwidth is adapted to the detuning of the corresponding HFI transition³. Here frequency mixers with 3 GHz bandwidth for the HFI repumper and 2.5 GHz for the HFI imaging laser lock are used. To suppress non-linear distortion effects (third-order inter-modulation) a high input level for the mixer (on the order of +13...+17 dBm) is needed [48]. Behind the bias Tee the RF-signal has a typical level of between about -30 ... -20 dBm. That is why two amplifiers increase the level by +40 dBm, so that a sufficient load for the mixer is ensured. A phase-locked voltage controlled oscillator (VCO) is used, with a bandwidth of 137.5 - 4400 MHz and a maximal output power of + 17 dBm. The frequency as well

-
- 2 The bias tee consists basically of a capacitor and an inductor. With the capacitor the AC signal is coupled while the DC bias is blocked (RF-port), whereas the inductor only allows passing the DC signal (DC-port). In addition the serial connection of capacitor and inductor works simultaneously as a low-pass filter, which separates both output ports from each other
 - 3 For the maximal accessible magnetic field of 1400 G the frequency shift of the repumper transition is 2986 MHz and of the imaging transition 1960 MHz.

3 High-field imaging system

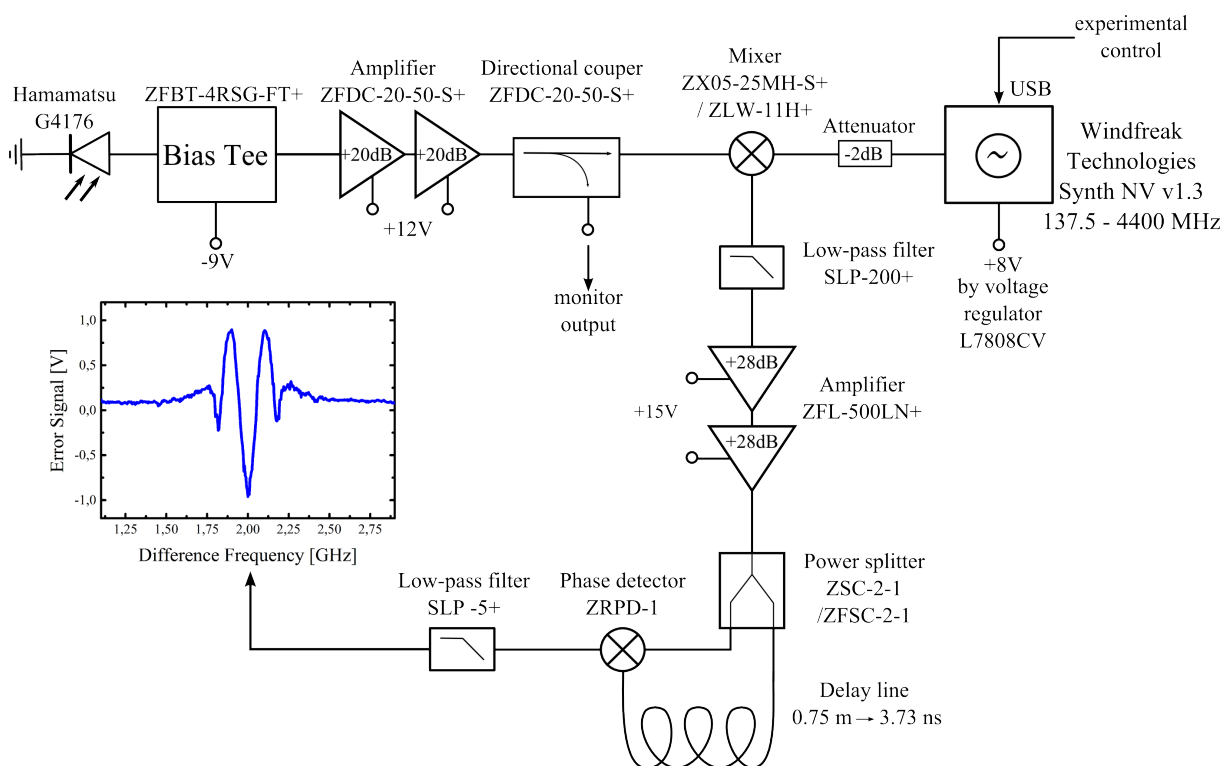


Figure 3.7: Setup for the offset beat lock. For the lock of the repumper laser another frequency mixer (ZLW-11H+, 3GHz bandwidth) is used as for the imaging laser (ZX-25MH-S+, 2.5 GHz bandwidth).

as the output level is controlled via USB directly by the experimental control. To protect the VCO from damages induced by reflection of high power RF signals, an additional 2dB - attenuator is implemented in front of its output. After mixing the optical beat with the VCO signal the high frequency part is suppressed by a low-pass filter with a cut-off frequency of 200 MHz. The difference signal ω_- is split by a 50:50 power splitter and recombined by a phase detector while one part is delayed by a coaxial cable. After this the DC part (see Eq. 3.5) is filtered out by a 5 MHz low-pass filter and is used as an error signal for the feedback loop.

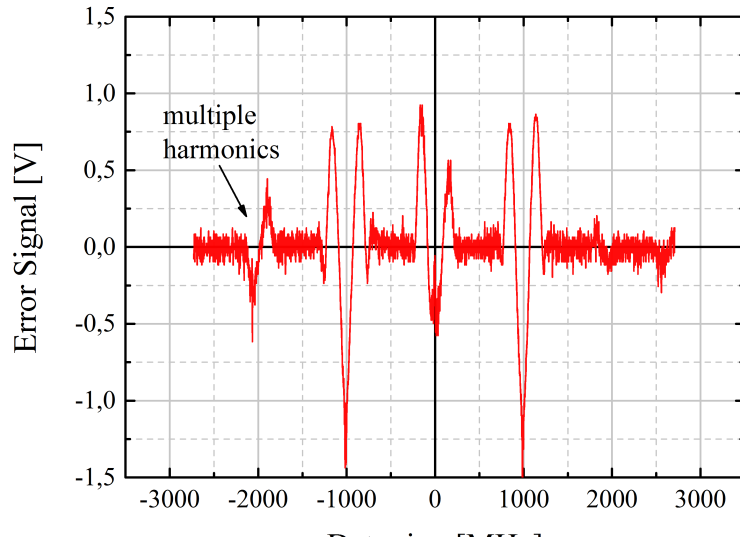
Error signal

In order to obtain a broad capture range, but still ensure an adequate steep slope a length of ~ 75 cm was chosen, which corresponds to a time delay of ~ 3.73 ns and a capture range of ca. $\pm 1/2\tau \simeq 134$ MHz. This leads to a slope of the error signal of 17(4) mV/MHz for the repumper and 16(7) mV/MHz for the imaging laser, respectively. In Fig. 3.8 and 3.9 typical error signals for both HFI lasers are presented. The master laser is locked, while the slave laser is tuned over a range of ~ 5 GHz, leading to the appearance of two error signals as described in Sec. 3.2.1 (see Fig. 3.6 (b)).

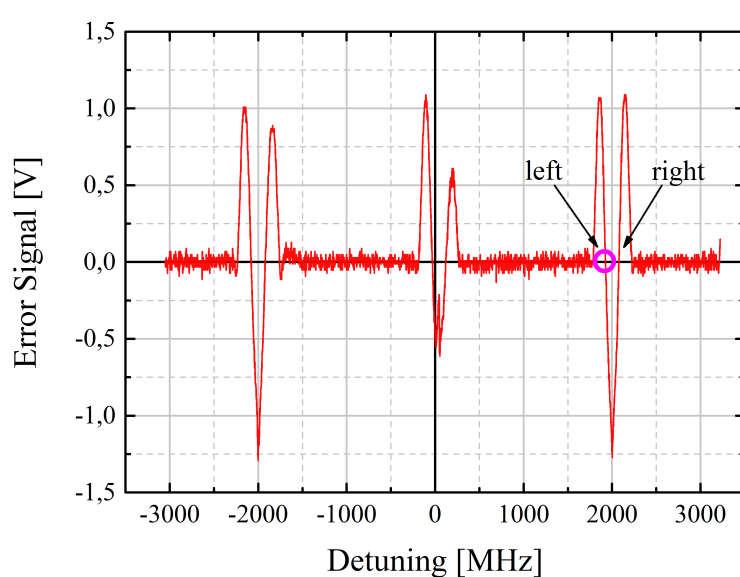
Furthermore, a third signature⁴ can be observed at zero detuning ($\omega_m = \omega_s$). It is still visible although the VCO is switched off, which indicates that it is generated by the beat-signal itself. The signature can be suppressed by a decrease of the beat-note's amplitude by means of reducing the laser power. However, this leads simultaneously to a decrease of the total error signal and also the steepness of the slope. Since this signature does not influence the locking and stability, the optical power of each beam is held to a value of 1 mW. Due to the fact that the VCO emits also higher harmonics, a further signature at multiples of the VCO frequency is generated, as visible in Fig. 3.8 (a). It occurs mainly for small VCO frequencies.

Locking on all zero-crossings is possible and has been tested successfully for different VCO frequencies. In the experiment, the error signal for positive detuning is used for both lasers. But the lasers are stabilized on different locking points represented by the purple and blue dot in Fig. 3.8 and Fig. 3.9, respectively. Due to the shape of the error signal, the locked laser frequency and therefore the beat signal shows a frequency offset related

⁴ A possible explanation for the appearance of this signature could be given by the broad width of the beat-signal. In general the frequency of the beat-note ($\omega_m - \omega_s$) should be zero in the resonance case $\omega_m = \omega_s$ preventing the creation of an error signal. But due to the broad width, a signal can be still detected by the photodiode. By passing the electronic circuit an error signal could be therefore produced.



(a) Error signal at 1 GHz



(b) Error signal at 2 GHz

Figure 3.8: Error signal for the imaging laser for different VCO frequencies. In the experiment, the falling slope of the signal for positive detuning is used for locking. It is marked by a purple dot. For the sake of simplicity the falling slope is denoted as the left, whereas the rising slope as the right slope.

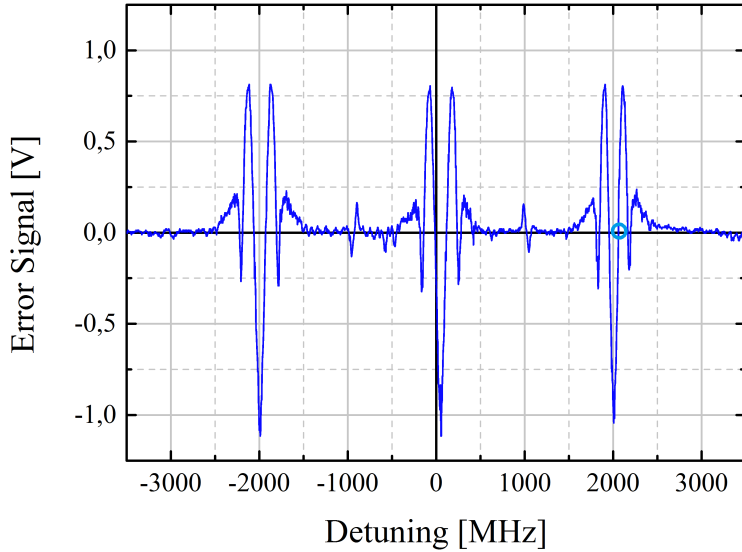


Figure 3.9: Error signal for the repumper laser at 2 GHz VCO frequency. The blue dot marks the locking point that is used in the experiment.

to the VCO set value. It behaves linearly and is either negative or positive depending on which locking point the laser is stabilized, as shown by the measurement in Fig. 3.10. The results of a linear fit are summarized in Tab. 3.1. The frequency offset becomes important, when the VCO frequency has to be calibrated for high-field imaging.

slave laser	left	right
HF imaging laser	-67.4(4) MHz	69.2(5) MHz
HF repumper laser	-59.2(5) MHz	59.3(6) MHz

Table 3.1: Offset of the beat frequency relative to the VCO set value (see Fig. 3.10).

3.2.3 Stability and noise

The laser system is stabilized by a so-called feedback loop. Its basic principle, is that the error signal is processed by a controller, which feeds back the output to the laser [49]. This controls the laser frequency, while suppressing noise and instabilities. With a proportional-integral-differential (PID) controller, a low-noise operation of the laser lock can be ensured. It consists of a differential input to prevent ground loops and a control unit, which regulates the signal that is fed back to the laser. For a detailed description of

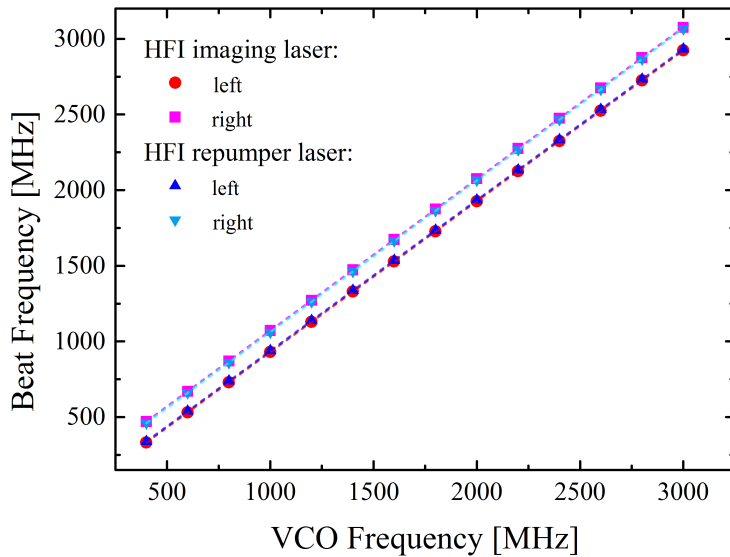


Figure 3.10: Beat frequency for different VCO set values. The HFI lasers have been locked on the right zero-crossing of the error signal, corresponding to the rising slope, as well as on the left one, corresponding to the falling slope (see Fig. 3.8 (b)).

feedback loops and their functional principle the reader is referred to different textbooks like reference [49] at this point.

Since we are using frequency offset locking, the stability of the high-field imaging system is dominated by the beat signal. Fluctuations of its frequency or width directly results in fluctuations of the imaging light. Therefore, the frequency locks of both HFI lasers have been analyzed in terms of stability and noise. First the used feedback loop in general is explained and characterized, followed by the analysis of the beat signal and its long-term stability. Furthermore, the noise spectrum has been measured and investigated, which is presented at the end of this section.

Feedback loop

In our setup a home-built PID controller (M1581) is used that feeds back the error signal to the control variable, the injection current of the HFI laser. Thus, the laser frequency is regulated. A schematic overview of the feedback loop is given in Fig. 3.11.

The PID settings are adjusted and optimized by modulating a step function onto the set value, the current of the laser diode, and reducing the response time of the system to its minimum. For a step function with an amplitude of 500 mV, one gets a response time

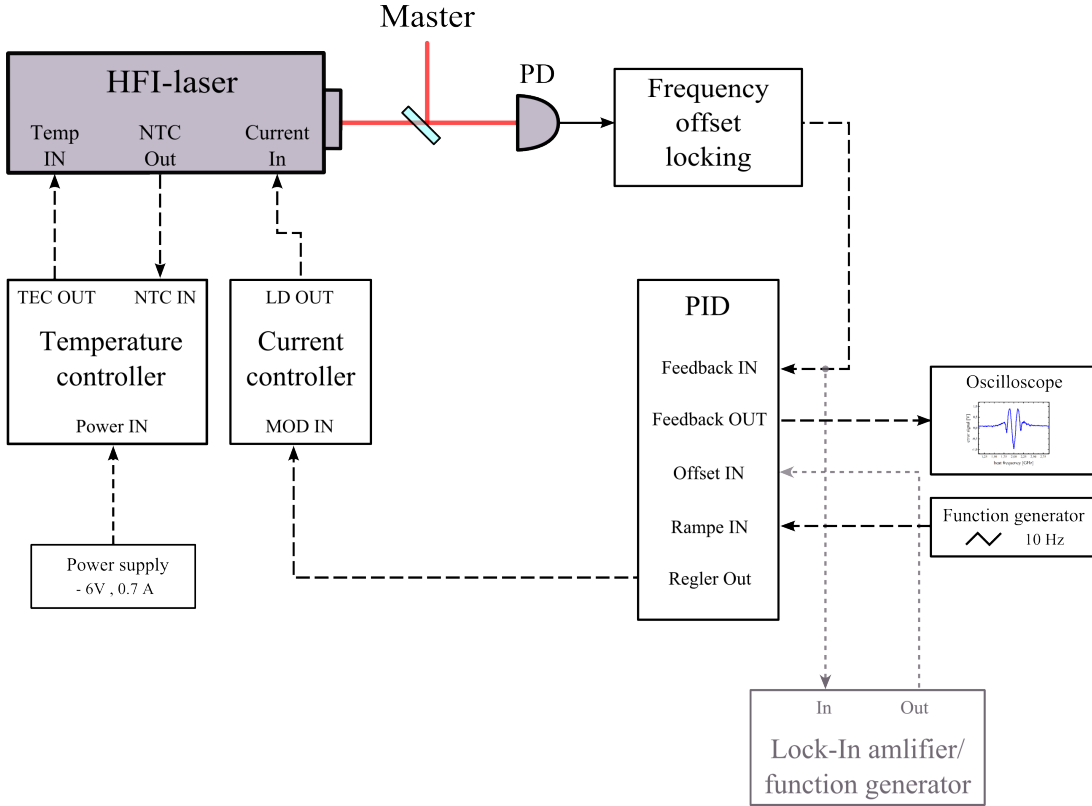


Figure 3.11: Overview of the servo loop.

of $\sim 12 \mu\text{s}$ for the imaging and $\sim 15 \mu\text{s}$ for the repumper laser lock.

The bandwidth of the feedback loop has been characterized with a lock-in amplifier. The set value is modulated by a low level excitation signal. A lock-in amplifier (STANFORD RESEARCH SYSTEMS, SR850 DSP) measures the phase and the amplitude of the system's response and compares it with the excitation signal. Thereby, the phase difference and amplitude frequency response can be directly measured. Plotted over the excitation frequency, one obtains the *Bode plots* [49], from which the feedback bandwidth can be directly determined. In our setup the injection current is modulated with a sinusoidal signal provided by a function generator, which is attached to the lock-in amplifier. The amplitude is adjusted to a constant value of $10 \text{ mV}_{\text{rms}}$ ($\sim 30 \text{ mV}_{\text{pp}}$), while the frequency

HFI laser	3dB-attenuation	$\pi/2$ -shift
Imaging	96.9(2) kHz	34.8(2) kHz
Repumper	84.7(2) kHz	37.0(2) kHz

Table 3.2: Servo bandwidth of the HFI laser lock setups. Due to the appearance of the servo bump the bandwidth is determined by the $\pi/2$ -shift.

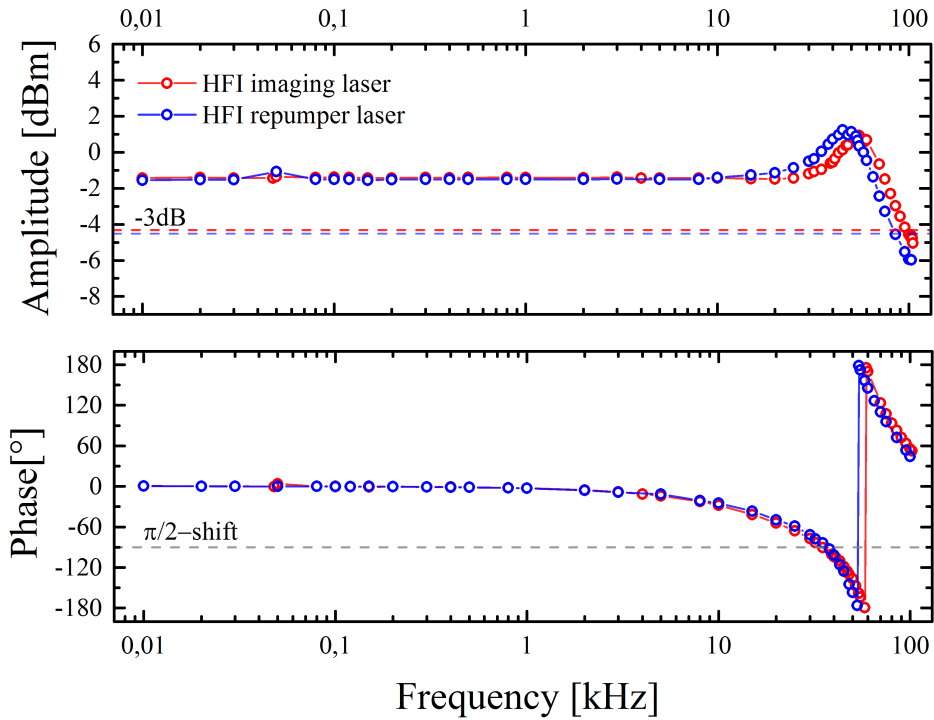


Figure 3.12: Bode plot for the locked servo loop. The upper image shows the gain response with the servo bump for both HFI laser, whereas the lower image represents the phase response. The bandwidth can be determined either by the 3dB-attenuation or the $\pi/2$ -shift.

is tuned up to 100 kHz. The implementation of the lock-in amplifier is shown in Fig. 3.11. During the whole measurement the HFI lasers are locked on a VCO frequency of 1000 MHz. The measured Bode plots for both lasers are presented in Fig. 3.12. At ~ 47.5 kHz and ~ 55 kHz for the repumper (blue) and imaging (red) laser, the so-called *servo bump* is visible. At these frequencies the negative feedback transforms into a positive feedback. This corresponds to a phase shift of 180° , which results in an amplification of the amplitude. It has to be noticed that the servo bump does not represent additional noise, but its sensitivity to noise around a critical frequency ω_c is enhanced [49]. This means, ω_c represents the upper limit of the regulated frequency regime. The bandwidth of a closed servo loop is defined by the 3dB-attenuation of the amplitude corresponding to a $\pi/2$ -shift in the phase response. Due to the appearance of the servo bump the determination by 3dB-attenuation is distorted. Therefore, the bandwidth has been estimated by the $\pi/2$ -shift, summarized in Tab. 3.2. In order to reduce the influence of technical or electronic noise on the laser stabilization as much as possible, the servo loop has been adjusted to its maximal bandwidth resulting $34.8(2)$ kHz and $37.0(2)$ kHz for the imaging

and repumper laser, respectively.

Beat signal

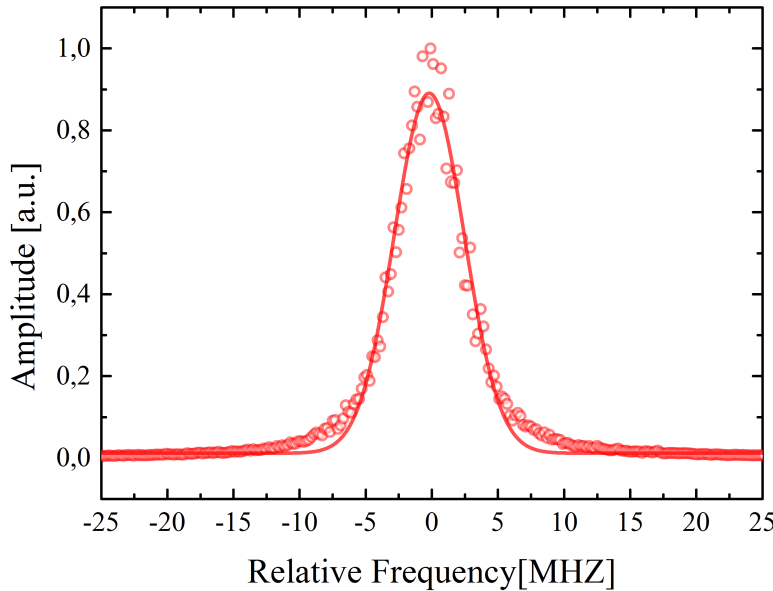
As mentioned before the beat signal is of an essential relevance for the frequency offset locking. A fluctuating beat-note leads to an instable performance of the high-field imaging. Therefore, the beat signal has been measured and characterized by means of its width. The measurements are shown in Fig. 3.13, where the lasers are locked on a VCO frequency of 1000 MHz. The beat signals have been recorded with a spectrum analyzer (RHODE & SCHWARZ, ZVL13 NETWORK ANALYZER) at the monitor output of the directional coupler (see Fig. 3.7). The sweep time (SWT) is set to 25 ms and the resolution bandwidth (RBW) to 300 kHz. The data points represent the average over 100 independent measurements, which are recorded consecutively. The amplitude is linearized and normalized to the signal's maximum. Afterwards the data are fitted with a Gaussian distribution to obtain the full width at half maximum (FWHM). The fit results are summarized in Tab. 3.3 and show a width of 6.23(5) MHz and 14.1(1) MHz for the imaging and repumper laser lock, respectively. The master lasers width (FWHM), that could be estimated to a Gaussian width of $\Delta\omega_{\text{master}} \approx 200$ kHz in a previous measurement (see diploma thesis of Stefan Schmidt [39]), is far below the determined FWHM. Therefore, it can be assumed that their influence on the beat signal is quite small and, hence, the DBR-lasers dominate. The laser linewidth can be estimated by means of the beat-note's FWHM, since it describes the convolution of the overlapped slave and master laser line shapes. By assuming Gaussian line shapes, one can deduce the DBR laser linewidths by

$$\Delta\omega_{\text{Beat}} = \sqrt{\Delta\omega_{\text{master}}^2 + \Delta\omega_{\text{slave}}^2} . \quad (3.6)$$

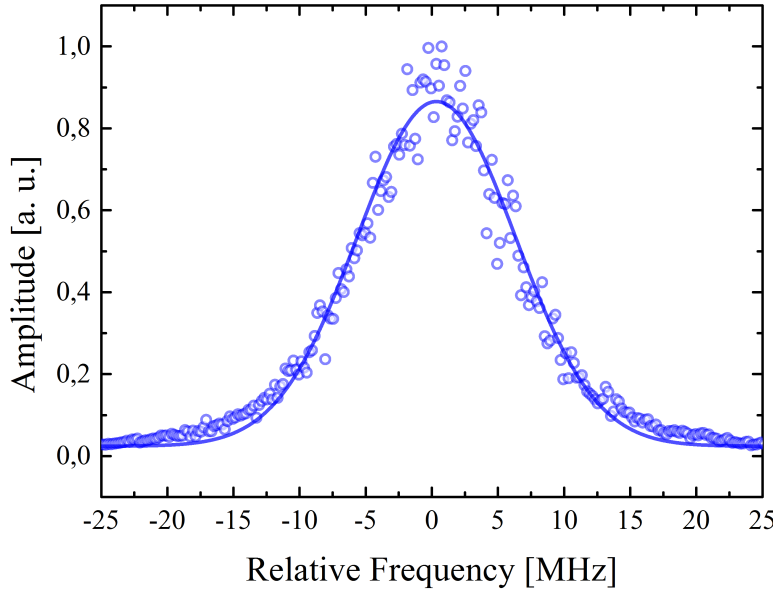
The obtained widths of ~ 6.2 MHz for the imaging laser and ~ 14.1 MHz agree with the fitted beat width and confirms that the beat and also the stability of the lock is dominated by the DBR-lasers. The obtained linewidth deviate significantly from each other, although the same model of laser diodes is used here. Since both lasers are home-

HFI laser	$\Delta\omega_{\text{L,Gauss}}$	R^2	χ^2_{red}
Imaging	6.23(5) MHz	0.98183	0.0006
Repumper	14.1(1) MHz	0.98209	0.0011

Table 3.3: FWHM of the beat signal for both HFI laser locked on 1000 MHz VCO frequency. The width is obtained by a fit with a Gaussian profile.



(a) Beat signal of the imaging laser with the *master cooler*



(b) Beat signal of the repumper with the *master repumper*

Figure 3.13: Beat signal with fit for both lasers locked at 1000 MHz. The beat-notes are measured with a spectrum analyzer at a resolution band width of 300 kHz and a sweep time of 25 ms. The data points (circles), which represent the mean over 100 independent measurements, are fitted to Gaussian distribution (solid lines).

built, it is likely that this deviation results from small differences in the technical setup, e.g. in the electronics. As a consequence additional noise is generated, which broadens the laser linewidth. The Gaussian fit does not perfectly fit to the data as one can see in Fig. 3.13 and also on the values of χ^2_{red} in Tab. 3.3. But due to less knowledge of the actual laser line shapes and the laser noise, an exact determination of the FWHM is not possible. Since the HFI lasers stay stable over ~ 2.5 s during the beat measurements, it shows that the frequency offset lock is suitable to perform stable HFI imaging on a timescale of a typical experimental sequences. But since measurements can take few minutes to hours, a stable laser lock is required also for long terms. For this reason the long-term stability has been investigated.

Long-term stability

As for the linewidth measurements the beat signal is recorded by a spectrum analyzer, while the HFI lasers are locked with an offset of 1000 MHz. Every 10 s a trace is recorded for a total of 10 min and fitted afterwards with a Gaussian distribution for each. By assuming a normal distribution of the resulting values, one can determine the mean beat frequency and the mean width. The fluctuations are estimated by the FWHM of the corresponding normal distribution.

The results show fluctuations on the order of ~ 1 MHz related to the mean beat frequency for both, the imaging and repumping laser lock, which is comparable to other frequency offset lock setups [29, 30]. The beat width, however, fluctuates by up to about 2 MHz for the repumper laser lock. These fluctuations are large compared to the obtained linewidth of ~ 6 MHz for the imaging and ~ 14 MHz for the repumping laser, respectively. High-field imaging will be therefore influenced, because the laser frequency will fluctuate around the transition frequency. Averaged over time, this can lead effectively to a broader laser linewidth yielding a reduced absorption of Cs atoms. But since the fluctuations are still smaller than the natural linewidth of the D₂-transition $\Gamma_{\text{D}_2} = 5.234$ MHz, absorption imaging of cesium atoms is possible. Additional long-term stability measurements of several hours were also investigated. The frequency offset locks remain stable over 12 hours and show fluctuations on the order of ~ 2 MHz $< \Gamma_{\text{D}_2}$.

Noise spectrum

In order to understand, which noise or disturbances influence the laser stabilization and linewidth, frequency fluctuations have been investigated. In the following, the concept of determining the noise spectrum, based on reference [50], is briefly explained.

3 High-field imaging system

The total power P of a light field $E(t)$ is proportional to the optical power spectral density (PSD)

$$P \propto \langle E^2(t) \rangle_t = \int S_E(f) df . \quad (3.7)$$

$S_E(f)df$ describes the average power of an electric field carried by frequencies between f and $f + \Delta f$. This means, that frequency fluctuations of a light field can be directly characterized by the PSD and, therefore, the linewidth of the light field is directly related to the spectral width of the PSD. It can be obtained by a Fourier analysis:

$$S_E(f) = 2 \lim_{T \rightarrow \infty} \frac{1}{T} \left| \int_0^T E(t) e^{-i2\pi ft} dt \right|^2 . \quad (3.8)$$

With the Wiener-Khinchin theorem, which states that the spectral density is the Fourier transform of its time-dependent autocorrelation function, the PSD can be described by

$$S_E(f) = 2 \int_0^\infty \langle E(t)E(t+\tau) \rangle_t e^{-i2\pi f\tau} d\tau . \quad (3.9)$$

The electric field $E(t)$ is given by

$$E(t) = E_0 \sin(\omega_0 t + \phi(t)) , \quad (3.10)$$

with the amplitude E_0 , carrier frequency ω_0 and the phase fluctuations $\phi(t)$. The instantaneous frequency is characterized by

$$\omega(t) = \omega_0 + \frac{d\phi(t)}{dt} = \omega_0 + \delta\omega(t) , \quad (3.11)$$

where $\delta\omega(t)$ describes a time-dependent frequency fluctuation, which vanishes for time-averaging $\langle \delta\omega(t) \rangle_t = 0$. Since the electric field is not directly dependent on frequency fluctuations $\delta\omega(t)$, a direct measurement is not possible. But by means of the instantaneous frequency in Eq. 3.11, frequency fluctuations can be measured in arbitrary short time intervals. Related to Eq. 3.8 and 3.9, one gets the spectral noise density (SND), which is given by

$$\begin{aligned} S_\nu(f) &= 2 \lim_{T \rightarrow \infty} \frac{1}{T} \left| \int_0^T \nu(t) e^{-i2\pi ft} dt \right|^2 \\ &= 2 \int_0^\infty \langle \nu(t)\nu(t+\tau) \rangle_t e^{-i2\pi f\tau} d\tau , \end{aligned} \quad (3.12)$$

with the frequency fluctuations $\nu(t) = \delta\omega(t)/2\pi$. It is described in units of Hz^2/Hz [50] and

its rms (root-mean-square) width $\Delta\nu_{\text{rmw}}$ is also directly related to the laser linewidth. The spectral noise density can be directly obtained by using the property of the error signal. Since we lock on a zero-crossing, a shift in voltage directly corresponds to a change in frequency (see Fig. 3.8 or 3.9). With the slope of the error signal it is possible now to convert between voltage and frequency fluctuations. Thus $\nu(t)$ can be directly measured and by using Eq. 3.12 the spectral noise density is determined.

With an oscilloscope (TEKTRONIX, TDS 2004B, 60 MHz), the voltage fluctuations of the lock signal are recorded for different timescales in a closed feedback loop. The measurements are done between 10 ms and 1 μs in decade steps sampling 2900 data in each case. Since five traces are recorded in every step, the data are first averaged and on the basis of Eq. 3.12 the autocorrelation function and its Fourier transform are calculated. For this the data are converted into the frequency space. In order to investigate the noise for different offset frequencies, the HFI lasers are locked with an offset of 500, 1000 and 2000 MHz. The results are presented in Fig. 3.14. Due to an almost identical locking setup for the HFI lasers, a similar behaviour of the spectral noise density is visible. Furthermore, the noise spectrum for locking at different VCO frequencies show in principle the same results, which means that the noise level and spectrum is equal for the whole VCO tuning range. This indicates that high-field imaging for all accessible magnetic fields is equally influenced by noise. The noise levels of both laser lock stay constant up to 4×10^4 Hz, which results from the servo loop. The peaks at about $\sim 40 - 50$ kHz describes the already mentioned servo bump. For higher frequencies both spectra show a drop at ~ 5 MHz, which corresponds to the low-pass filter at the end of the offset lock circuit (see Sec. 3.2.2). Furthermore, some characteristic noise occurs at ~ 240 kHz, ~ 2.5 MHz and ~ 5 MHz. The exact origin is up to now unknown, but it is likely electronically induced. A low-pass filter with a smaller bandwidth could suppress it.

The noise level for the repumper lock (Fig. 3.14) is around $\sim 3 \times 10^5$ Hz²/Hz, whereas the imaging laser's lock shows a noise level of $\sim 6 \times 10^4$ Hz²/Hz, which is comparable to other locks used in our experiment [51, 39]. The discrepancy can be assigned to the difference in the laser linewidths, because the noise is directly related to the laser line shape [52, 53]. A broader laser line shape leads to a higher noise level and vice versa. This means that the noise and also the stability of the system are dominated by the broad laser linewidth of the DBR lasers. In order to prevent the limitation by the laser system a new narrow-band laser⁵ has been tested with promising results. Further details are given in appendix B.

⁵ NarrowDiode by Radiant Dyes with a laser linewidth of ~ 20 kHz

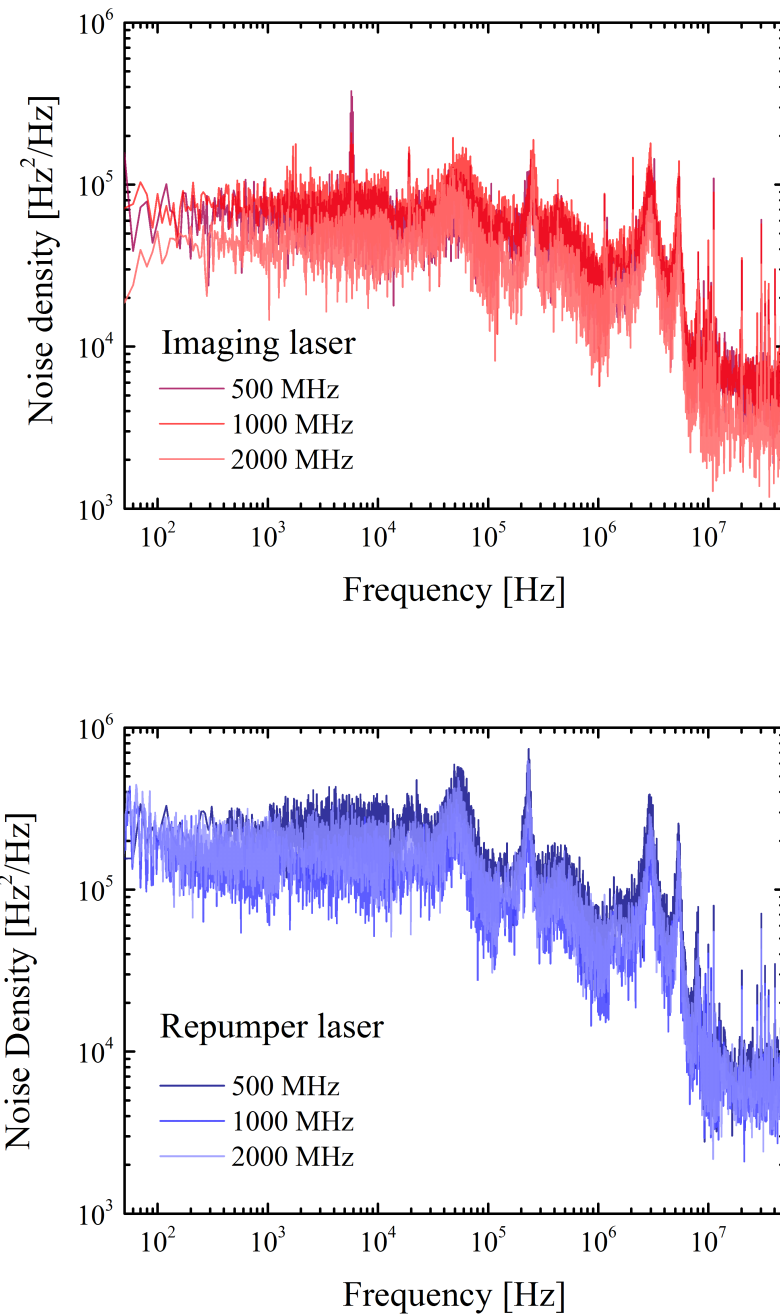


Figure 3.14: Spectral noise density of both HFI laser locks. The imaging (red) and repumper (blue) laser are stabilized with different offset frequencies.

4. Absorption imaging of Cesium atoms

Absorption imaging of cold atoms gives access to physical quantities of the atomic cloud. From its spatial density distribution, characteristic properties can be determined, such as atom number, density, temperature and trapping frequencies. In order to obtain precise values, a stable and precise absorption imaging is required. Therefore, the high-field imaging system has been characterized by comparing absorption of Cs atoms with a reference system, for which the low-field imaging system has been used. The results are presented in this chapter.

First in Sec. 4.1, a brief introduction into our absorption imaging setup and an overview of the diagnostics and the experimental procedure is given. Afterwards the high-field imaging system is characterized, starting with the comparison with the low-field imaging system in Sec. 4.2. Finally, imaging of Cs atoms at high magnetic fields is realized successfully and presented in the last Sec. 4.3.

4.1 Absorption imaging

There are different possibilities of absorption imaging¹, e.g. the in-situ and time-of-flight (TOF) imaging, where atoms are imaged while being in a trap or while expanding after release from the trap, respectively [54]. In our experimental setup TOF imaging is used, which can be carried out in the vertical as well as in the horizontal plane. For the results in this thesis, the horizontal direction has been used. The absorption imaging system is built up, so that it projects a 1:1 image on the CCD camera². For a detailed description of the imaging setup the reader is referred to previous theses [39, 40].

¹ Imaging of atoms by absorption is a destructive technique. If required, non-destructive techniques can be used, which are based on the dispersive character of a dilute gas, such as phase- or polarization-contrast imaging for instance.

² Both Guppy-38B, Allied Vision Technology

Determination of the atom number

An atomic cloud, characterized by the particle density $n(x, y, z)$, is illuminated by a resonant laser beam and its shadow is imaged on a CCD-camera. The measured intensity distribution $I(x, y)$ of the shadow image is described by the Lambert-Beer law:

$$I(x, y) = I_0(x, y) \exp(-od(x, y)) , \quad (4.1)$$

where $I_0(x, y)$ is the initial intensity and $od(x, y)$ the optical density per camera pixel³ at position (x, y) , which is defined as the product of the atomic absorption cross section σ and the column density $\eta(x, y)$:

$$od(x, y) = \sigma \cdot \eta(x, y) . \quad (4.2)$$

The column density is the particle density $n(x, y, z)$ integrated over the z-direction: $\eta(x, y) = \int n(x, y, z) dz$.

While measuring the transmitted intensity distribution $I(x, y)$, background or scattered probe light can distort the measurement [54]. In order to prevent the influence of the imperfect environment, three images are taken. The first one is the absorption image $I_{\text{abs}}(x, y)$, where the atomic cloud is illuminated with a resonant laser. The second one, the so-called division image $I_{\text{div}}(x, y)$, is taken under the same conditions, but without atoms. Finally a third image is recorded without laser beams, the so-called background image $I_{\text{bg}}(x, y)$ [54, 40] (see Fig. 4.2). The subtraction of $I_{\text{bg}}(x, y)$ from the other images leads therefore to the elimination of the background light. By dividing both corrected images, one gets the relative transmission $T(x, y)$:

$$T(x, y) = \frac{I(x, y)}{I_0(x, y)} = \frac{I_{\text{abs}}(x, y) - I_{\text{bg}}(x, y)}{I_{\text{div}}(x, y) - I_{\text{bg}}(x, y)} . \quad (4.3)$$

Thus it is possible to determine the optical density

$$od(x, y) = -\ln(T(x, y)) \quad (4.4)$$

and hence the column density

$$\eta(x, y) = -\frac{\ln(T(x, y))}{\sigma} . \quad (4.5)$$

³ Effective pixel size: $7.84 \mu\text{m} \times 18.4 \mu\text{m}$

The peak optical density, as well as the atom number, is obtained now by fitting a two dimensional density profile to $od(x, y)$. For a thermal cloud, which is the case for the following results, that is centered at (x_0, y_0) and tilted by θ with respect to the camera, the following Gaussian profile can be used:

$$od(x, y) = od_0 \cdot e^{-[\alpha(x-x_0)^2 + 2\beta(x-x_0)(y-y_0) + \gamma(y-y_0)^2]} , \quad (4.6)$$

where od_0 is the peak optical density and α , β and γ are coefficients⁴ depending on the tilt θ [40]. The atom number can be obtained by approximating that it corresponds to the product of the peak column density $\eta_0 = od_{\max}/\sigma$ and the volume of the atomic cloud V_{Gauss} , which is described by a Gaussian distribution: $N = \eta_0 \cdot V_{\text{Gauss}}$. Thus, one gets the total atom number by

$$N = \frac{od_0}{\sigma} 2\pi \Delta_x \Delta_y , \quad (4.7)$$

with the $1/e^2$ radii Δ_x and Δ_y obtained from the Gaussian fit in Eq. 4.6.

Absorption cross section

Since the atom number depends on the absorption cross section, it is important to know about its correct value. In the resonant case the cross section is given by [36]:

$$\sigma_0 = \hbar\omega_0 \cdot \frac{\Gamma}{2I_{\text{sat}}} , \quad (4.8)$$

where $I_{\text{sat}} = \frac{\hbar\omega_0^3\Gamma}{12\pi c^2}$ describes the saturation intensity, ω_0 the resonant transition frequency, and Γ the natural linewidth, in our case $\Gamma_{D_2} = 5.234$ MHz. Since we are using the σ^+ -transition $F = 4 \rightarrow F' = 5$ for imaging at zero field, this simplifies to

$$\sigma_0 = \frac{3\lambda^2}{2\pi} = 3.469 \times 10^{-9} \text{ cm}^2 , \quad (4.9)$$

with $I_{\text{sat}} = 1.1049 \text{ mW/cm}^2$ according to reference [36].

For high magnetic fields, however, the resonant cross section has to be corrected. This is due to the fact that the magnetic field, which defines the quantization axis, is oriented in z-direction. The imaging, however, is applied with σ^+ -light in horizontal plane, that means perpendicular to the magnetic field. Regarding the projections on the quantization axis this leads to a reduction of a factor of four. Besides the leakage rate of 6 % of the

⁴ $\alpha = \frac{\cos^2(\theta)}{2\Delta_x^2} + \frac{\sin^2(\theta)}{2\Delta_y^2}$, $\beta = -\frac{\cos(2\theta)}{4\Delta_x^2} + \frac{\sin(2\theta)}{4\Delta_y^2}$, $\gamma = \frac{\sin^2(\theta)}{2\Delta_x^2} + \frac{\cos^2(\theta)}{2\Delta_y^2}$

4 Absorption imaging of Cesium atoms

repumping transition $|F = 3, m_F = 3\rangle \rightarrow |m_I = 7/2, m_J = 1/2\rangle$ has to be considered, as described in Sec. 2.3. Taking the leakage rate into account, this results in a fraction of 0.94 of the total number of atoms [37]. The resultant effective resonant cross section is thus given by

$$\sigma = \sigma_0 \times \underbrace{0.25}_{\text{projections on quant. axis}} \times \underbrace{0.94}_{\text{leakage}} = 0.815 \times 10^{-9} \text{ cm}^2. \quad (4.10)$$

The saturation intensity increases consequently by a factor of ~ 4 , since it is directly related to the resonant cross section: $I_{\text{sat,eff}} \simeq 4 \times I_{\text{sat}} \simeq 4.42 \text{ mW/cm}^2$.

Important for the following experimental results is also the off-resonant cross section, which is defined by

$$\sigma(\delta, I_L) = \frac{\sigma_0}{1 + (2\delta/\Gamma)^2 + (I_L/I_{\text{sat,eff}})}. \quad (4.11)$$

The cross section has a Lorentz profile and is depending on the detuning $\delta = \omega_L - \omega_0$ of the laser frequency ω_L from the resonance ω_0 and the laser intensity I_L . In the experiment I_L is adjusted well below the saturation intensity $I_L < I_{\text{sat}}$, in order to prevent broadening effects induced by a saturation. Thus, Eq. 4.11 simplifies to

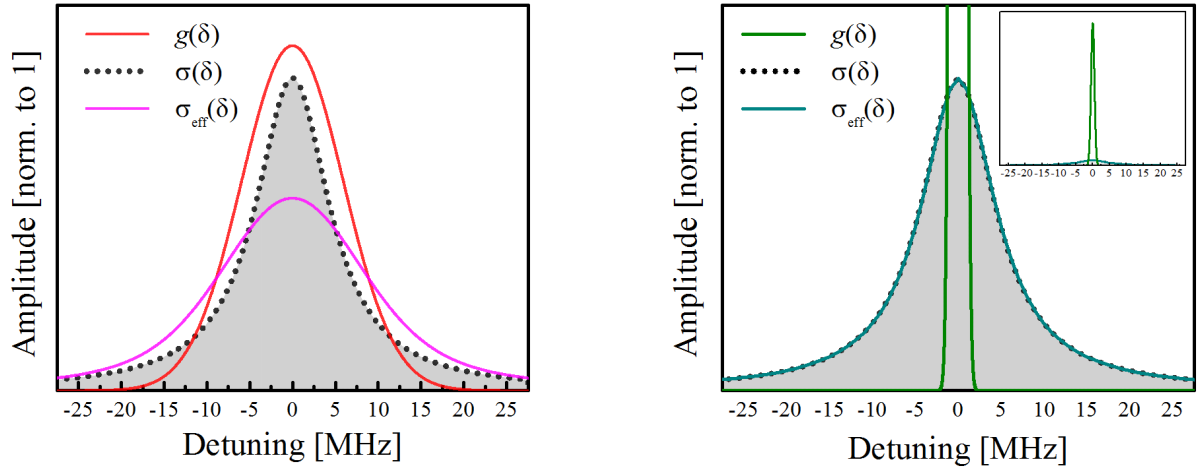
$$\sigma(\delta) = \frac{\sigma}{1 + (2\delta/\Gamma)^2}. \quad (4.12)$$

Experimentally the laser frequency and hence the detuning is scanned to obtain the resonant case. Thus, the Lorentzian shape of the absorption emerges, since the optical density od is proportional to $\sigma(\delta)$: $od(\delta) \propto \sigma(\delta)$.

Influence of the laser linewidth

Absorption imaging is hardly influenced by the laser linewidth, when using a narrow-band lasers, since their linewidths are much smaller as the natural linewidth: $\Delta\omega_L \ll \Gamma_{D_2} = 5.234 \text{ MHz}$. According to Eq. 4.12 the absorption cross section $\sigma(\delta)$ becomes comparable to the resonant cross section σ_0 . This is the case for the low-field imaging (LFI) setup, where the *master cooler* is used with a laser linewidth of $\sim 200 \text{ kHz} \ll 5.234 \text{ MHz}$. For high-field imaging, however, the influence of the laser linewidth cannot be neglected anymore since the DBR-lasers linewidth $\Delta\omega_L$ is greater than the natural linewidth: $\Delta\omega_L > \Gamma_{D_2}$. In this case an effective cross section is given by the convolution of $\sigma(\delta)$ with the laser lineshape $g_L(\delta)$:

$$\sigma_{\text{eff}}(\delta) = \int_{-\infty}^{+\infty} \sigma(\delta') \cdot g_L(\delta - \delta') d\delta', \quad (4.13)$$



(a) Effective cross section for the HFI system.
A laser linewidth of 6 MHz is assumed.

(b) Effective cross section for the LFI system.
The laser linewidth is 0.2 MHz.

Figure 4.1: Influence of the laser linewidth on the absorption cross section. The figures show the simulation of the effective cross section $\sigma_{\text{eff}}(\delta)$ for a broad laser linewidth in (a) and for a narrow laser linewidth in (b). $g(\delta)$ describes the Gaussian laser lineshape function and $\sigma(\delta)$ the off-resonant absorption cross section. The simulation predicts that for a broad laser linewidth (a) the cross section at resonance reduces: $\sigma_{\text{eff}}(0) < \sigma(0)$. For a narrow laser lineshape, however, the effective cross section does not change $\sigma_{\text{eff}}(\delta) = \sigma(\delta)$.

where δ describes the detuning from resonance. If one assumes a Gaussian laser lineshape, the effective cross section $\sigma_{\text{eff}}(\delta)$ is specified by a Voigt profile as depicted in Fig. 4.1. It shows the estimation of the resultant effective cross section $\sigma_{\text{eff}}(\delta)$ for two cases, a broadband and a narrow-band laser lineshape according to Eq. 4.13. Picture (a) shows the case of the imaging laser with a Gaussian linewidth of ~ 6 MHz and picture (b) the case of the *master cooler* with a linewidth of ~ 200 kHz. In both cases the Gaussian laser lineshape $g_L(\delta)$ as well as the Lorentzian cross section $\sigma(\delta)$ are normalized, so that the integral equals 1. The simulation shows that for the case of a broad laser linewidth in Fig. 4.1 (a), the effective absorption cross section at resonance $\sigma_{\text{eff}}(\delta = 0)$ becomes smaller than for the case of a narrow-band laser in Fig. 4.1 (b), where the cross section remains unchanged. Thus, one expects to observe less optical density in the experiment with the high-field imaging compared to the LFI system. Furthermore the resulting linewidth (FWHM) $\Delta\omega_V$ also changes in the case of a broad laser linewidth. According to Olivero *et al.* [55], it can be obtained by:

$$\Delta\omega_V \simeq 0.5346 \cdot \Gamma_{D_2} + \sqrt{0.2166 \cdot (\Gamma_{D_2})^2 + \Delta\omega_{\text{Laser}}^2}. \quad (4.14)$$

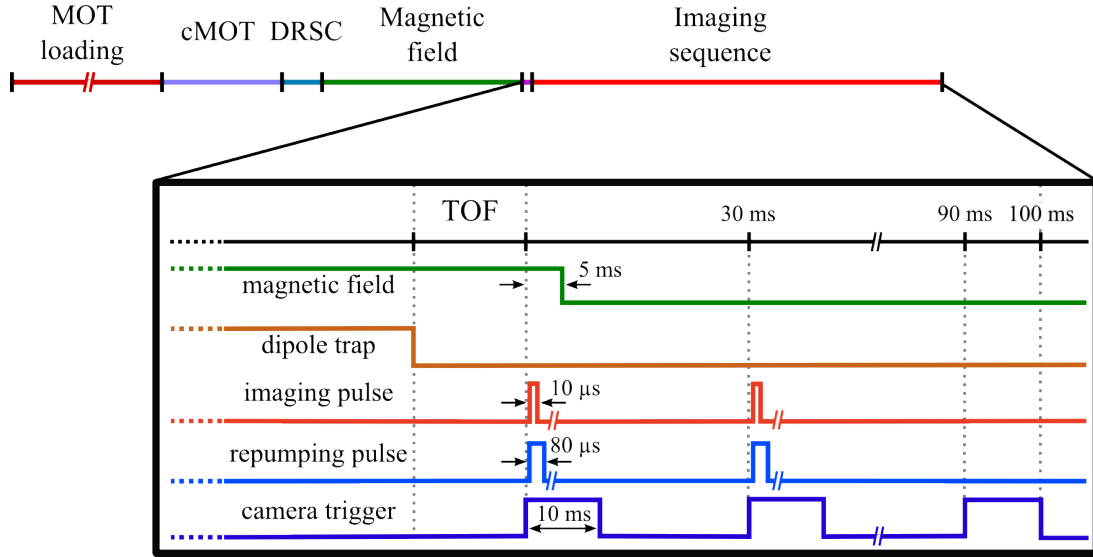


Figure 4.2: Typical sequence for imaging Cs atoms. At high magnetic field the atoms are imaged after leaving the optical dipole trap (ODT), whereas at zero field they are imaged after the compressed MOT phase (cMOT). In both cases the same imaging sequence is applied. Here three pictures are recorded. First, the absorption image, 30 ms later, the division image and the background image after 90 ms. The repumper light is shone in simultaneously with the imaging pulse. Further details are given in the text.

Experimental procedure

In the following a brief overview of the measurement procedure for experiments at high magnetic fields is given. But since here basically standard sequences are used, which were already used in previous experiments [20], I want to refer to the PhD thesis by Marc Repp [40] for further details.

Cs atoms are slowed down by a Zeeman slower and loaded into a magneto-optical trap [56] for 1 s. After a compression phase and degenerate Raman sideband cooling (DRSC) the atoms are brought into an optical dipole trap (ODT) [10]. The MOT is loaded at a displaced position from the center of the ODT. In the MOT phase typically $N_{\text{Cs}} \approx 2 \cdot 10^8$ atoms are trapped and cooled down to several hundred μK [40]. Afterwards the atoms are further cooled by a compression phase [57] and degenerate Raman sideband cooling (DRSC)[58] to a temperature of typically $T_{\text{Cs}} \approx 1 \mu\text{K}$. Here the atom numbers reduces to $N_{\text{Cs}} \approx 7 \cdot 10^7$ and $N_{\text{Cs}} \approx 2 \cdot 10^7$, respectively. In the compression phase the detuning of the MOT beams is increased, while an additional magnetic field gradient is ramped up simultaneously. Thus, the coldest atoms are spatially squeezed in a so-called compressed MOT (cMOT) and, hence, cooling below the Doppler limit is possible [57]. During the compression phase, the atoms are shifted by an offset field to the place of the ODT. Here

now the atoms are cooled down by DRSC and loaded simultaneously into the dipole trap. This cooling and loading sequence is applied for ca. 40 ms, which is divided in 30 ms for the compression phase and 10 ms for the DRSC. The atom number reduces during this process to about $10^4 - 10^5$ atoms with a temperature of typically few μK . After trapping in the ODT (detailed description of the dipole trap is given in previous thesis by Robert Heck [59]), a homogeneous magnetic field of arbitrary field strength is applied, in our case, for 50 ms, which splits the hyperfine states into their magnetic sub-levels. Finally the dipole trap is switched off, while the magnetic offset field stays on. Therefore, the atoms expand ballistically for a certain time-of-flight (TOF), typically few ms, until they are detected via absorption imaging. Here the imaging sequence is applied, in which three pictures are recorded, the absorption, the division and the background image. The length of the imaging pulse is 10 μs in each case, while the repumper is shone in for 80 μs simultaneously. The exact imaging sequence is presented and specified in Fig. 4.2. In contrast to imaging at high magnetic fields, atoms in a zero field have been imaged after the compression phase in this thesis, whereby more atoms are available, as depicted in Fig. 4.3. The figure shows two typical recorded absorption images in false colors. In the left figure (a) atoms after the compression phase are shown, whereas the right one (b) shows atoms after holding in the ODT.

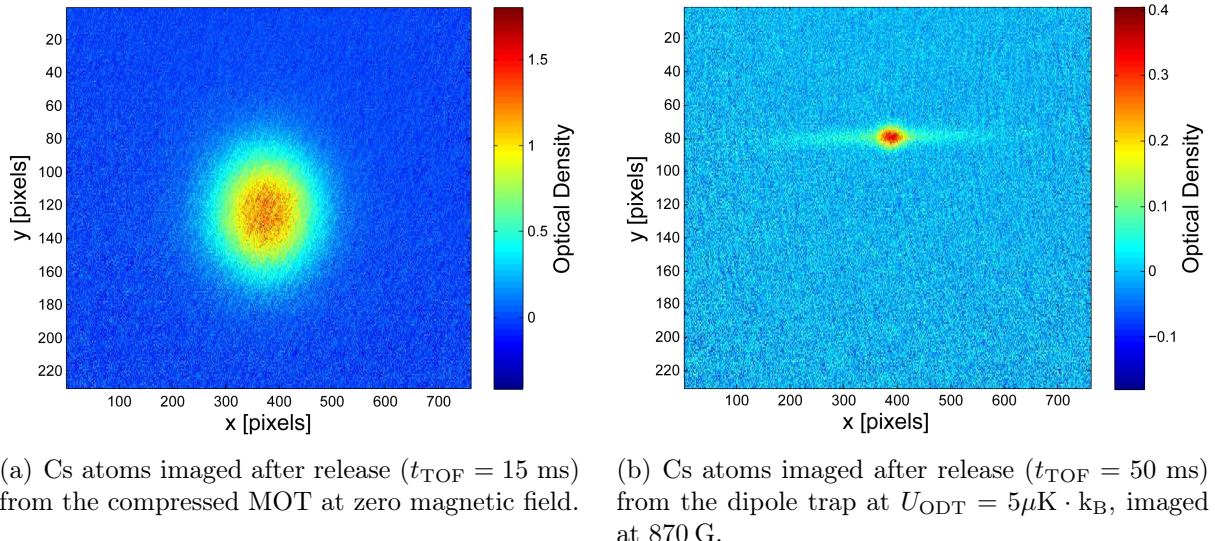


Figure 4.3: Absorption image (in false colors) of Cs atoms at zero (a) and high (b) magnetic field. The image is deduced by the method described in Sec 4.1. Because of the different conditions for imaging, both images are presented on different color scales.

4.2 Comparison with a reference system

In order to test the functionality as well as the efficiency of the high-field imaging (HFI) system, it is compared with the low-field imaging (LFI) system. In the following, measurements are presented, where Cs atoms have been observed at zero magnetic field with both imaging setups.

Scan of imaging lasers

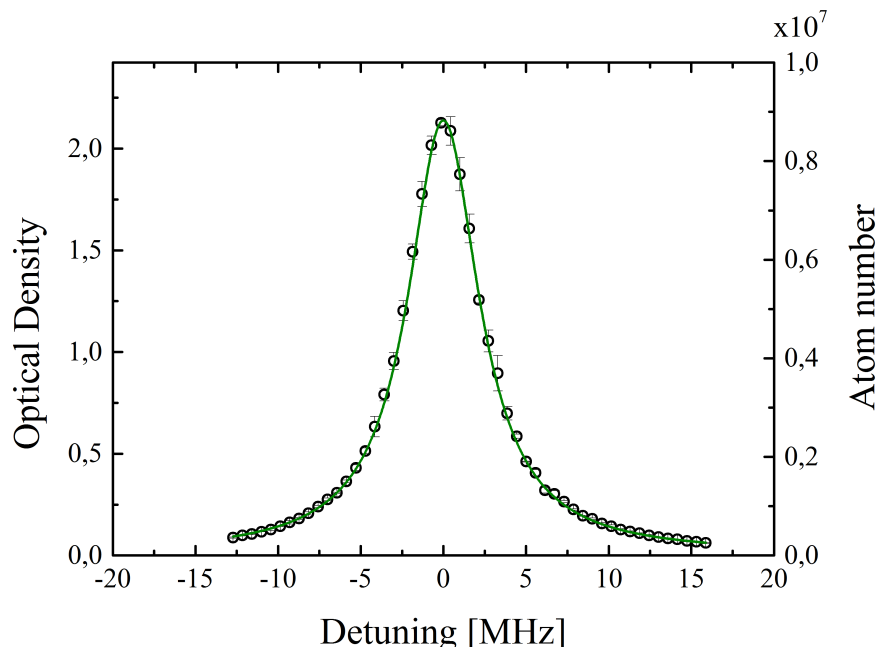
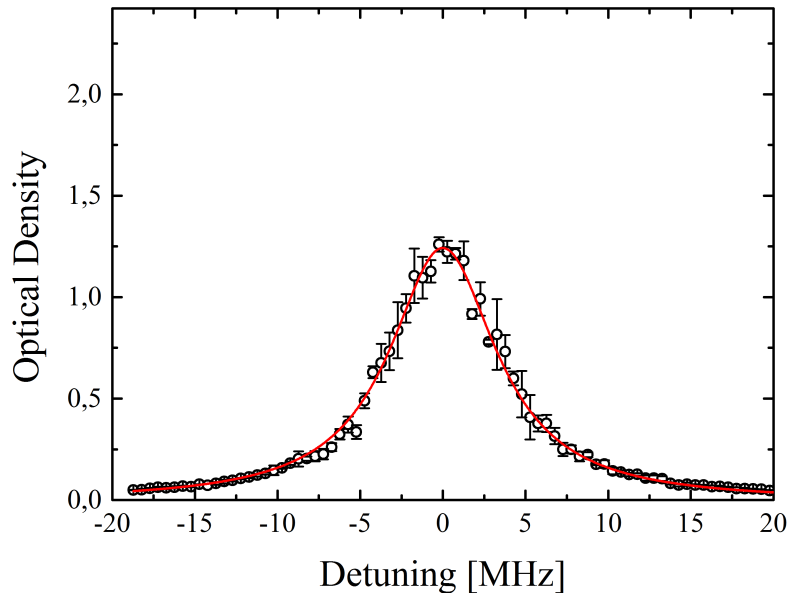
The experimental procedure follows the principle described in Sec. 4.1 with the main difference that the atomic cloud is detected after the compression phase and not in the optical dipole trap. The MOT is loaded only for 100 ms, resulting in a smaller particle number. After compression for 30 ms the atoms expand for $t_{\text{TOF}} \approx 15$ ms until they are imaged by either the low- or the high-field imaging system. The laser intensity in both cases is adjusted to a value well below the saturation intensity I_{sat} . To enable a precise comparison, in both cases the *master repumper*⁵ is used. However, the measurement is repeated again with the high-field repumper laser to test the high-field imaging system itself. In order to reach the imaging transition $F = 4 \rightarrow F' = 5$ and hence maximal absorption, the laser frequencies are scanned, the high-field imaging laser by tuning the VCO and the *master cooler* by tuning the AOM (see Fig. 3.4).

Both scans are presented in Fig. 4.4. The upper image (a) shows imaging with the LFI setup and the lower image (b) with the HFI setup. Here the atom number and the optical density in one dimension are presented depending on the detuning from resonance. The data points, describe the mean atom number over four measurements with its error bars⁶. In the case of LFI (Fig. 4.4 (a)), a Lorentzian curve is fitted to the data, described by the green curve, whereas a Voigt profile is used for HFI, described by the red curve. The obtained fit results are summarized in Tab. 4.1.

The amount of observed atoms in Fig 4.4 (a) is smaller than the expected order of magnitude of few 10^7 atoms as mentioned in Sec. 4.1. This is due to the smaller MOT loading time of 100 ms (usually 1 s). As predicted the optical density reduces when using HFI compared to the LFI system. This can be explained by the broader laser linewidth of the high-field laser as well as by fluctuations of the frequency lock on the order of 1-2 MHz. The effective cross section $\sigma_{\text{eff}}(\delta)$ (see Sec. 4.1) reduces at resonance $\delta = 0$ and consequently also the peak optical density according to Eq. 4.2. Thus, the atom number

⁵ Laser linewidth: $\Delta\omega_L \approx 300$ kHz [39]

⁶ The error bars represent the standard deviation for each data point.

(a) Scan of the *master cooler*

(b) Scan of the imaging laser

Figure 4.4: Imaging at zero magnetic field with the low-field(LFI) and the high-field imaging(HFI) setup, respectively. The images show a scan of the corresponding laser over the resonance of the transition $F = 4 \rightarrow F' = 5$. The data represent the average of four traces, which are fitted by a Lorentzian profile (red curve) for the case of LFI and by a Voigt profile in the case of HFI. This results in a width of 5.23(3)MHz for the absorption profile when imaging with the *master cooler* and 8.0(2)MHz with the imaging laser. In both cases the *master repumper* is used for repumping.

4 Absorption imaging of Cesium atoms

is underestimated by 40 %. But by comparing values of the fitted FWHM (deduced from the fit values in Tab. 4.1), one obtains the factor

$$C_{\text{corr}} \approx 1.53(4) ,$$

with which the atom number can be corrected.

Setup	Laser	od_0	FWHM [MHz]	R^2	χ^2_{red}
low-field	master cooler	2.13(2)	5.23(3)	0.999	1.642
high-field	imaging laser	1.25(1)	8.0(2)	0.993	0.002
	repumper laser	-	14.3(4)	0.986	0.780

Table 4.1: Experimental results of imaging with the low- and high-field imaging setup at zero magnetic field. The FWHM is obtained by fitting with a Lorentzian for LFI and a Voigt profile for HFI. The fits show a good agreement to the data as one can see on the values of R^2 and χ^2_{red} . Further details are explained in the text.

The fitted values for FWHM in Tab. 4.1 show the expected behaviour. Imaging with the LFI setup results in a FWHM of $\Delta\omega_{\text{LFI}} = 5.23(3)$ MHz, equal to the natural linewidth of the D_2 -transition $\Gamma_{D_2} \approx 5.234$ MHz. Imaging with the HFI setup, however, results in a broader FWHM of $\Delta\omega_{\text{HFI}} = 8.0(2)$ MHz, due to the broad linewidth of $\Delta\omega_{\text{L,Beat}} \approx 6.2$ MHz (see Ch. 3) of the imaging laser, as explained in Sec. 4.1. By using Eq. 4.14 the laser linewidth can be estimated, resulting in a width of $\Delta\omega_{\text{L}} \approx 4.6(2)$ MHz, which is smaller but comparable with the estimated laser linewidth from the beat measurement.

Scan of repumper laser

The presented measurements have been performed so far only by use of the *master repumper*. But to test the high-field imaging system itself, the measurement has been repeated while pumping with the high-field repumper laser. Here the imaging laser is stabilized on a fixed VCO value⁷ corresponding to maximal absorption (obtained by the measurement in Fig. 4.4 (b)) while scanning the repumper frequency over the resonance of the repumping transition $F = 3 \rightarrow F' = 4$. The scan is shown in Fig. 4.5, where the absorption is presented in the relative cross section $\sigma(\delta)/\sigma_0$ and not as before by means of optical density. This is due to an error in the experimental sequence. While measuring with the high-field imaging laser, the *master cooler* has been also shone onto the atomic cloud and onto the camera, which leads to an higher incident intensity and a

⁷ VCO: 793.84 MHz, Beat: 850 MHz

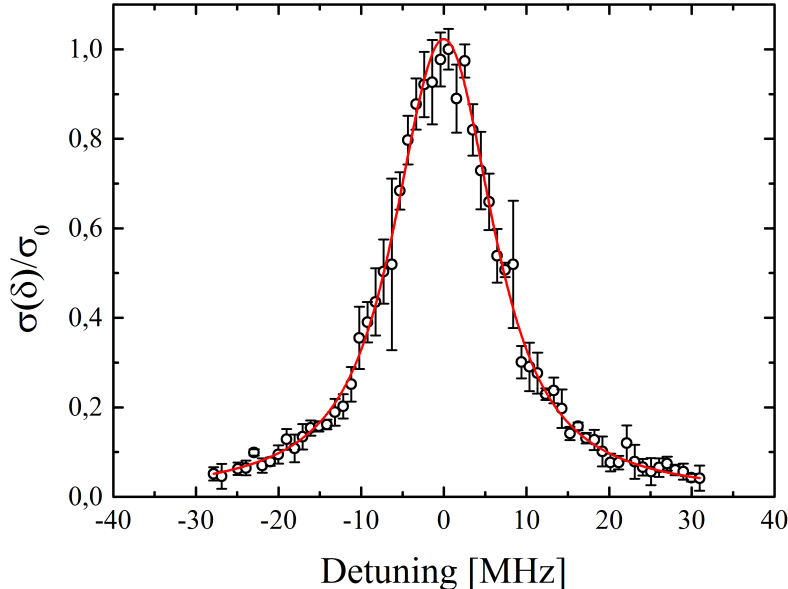


Figure 4.5: Scan of the repumper laser. Since the *master repumper* is used for the measurement in Fig. 4.4, here the repumper is scanned over the transition $F = 3 \rightarrow F' = 4$. Simultaneously the imaging laser is locked to resonance of transition $F = 4 \rightarrow F' = 5$, so that atoms can be imaged. The data are represented in relative absorption $\sigma(\delta)/\sigma(0)$. For details see text.

brighter background image. According to Eq. 4.4, therefore, the obtained optical density is increased, so that it is not feasible to extract the correct values for the actual optical density. However, the FWHM can be obtained by normalizing the data to its peak optical density $od(\delta)/od_{\max}$. Thus, the actual shape of the absorption profile emerges, since $od(\delta)$ is proportional to $\sigma(\delta)$, according to Eq. 4.2. Through a Voigt fit to the data, one gets a $\Delta\omega_{\text{HFII}} = 14.3(3)$ MHz for the repumper laser. This is comparable to the laser linewidth of $\Delta\omega_L \approx 14.1$ MHz estimated by the beat-note measurement in Sec. 3.2. As before one can estimate the laser linewidth from the fitted FWHM $\Delta\omega_{\text{HFI-REP}} = 11.2(4)$ MHz, which is in the same regime as obtained by the beat measurement in Sec. 3.2.3.

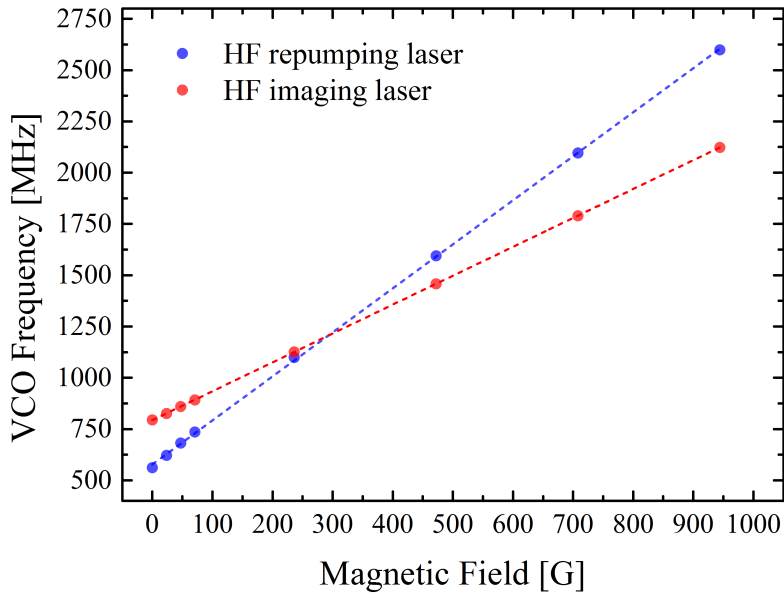


Figure 4.6: Calibration of the VCO frequency on the magnetic field.

4.3 Imaging at high magnetic fields

For imaging of Cs atoms in high magnetic fields the atoms are held in the optical dipole trap. This allows to manipulate atoms by an external magnetic offset field. The experimental procedure follows the scheme described in Sec. 4.1. The atoms are imaged after $t_{\text{TOF}} = 4$ ms with the HFI laser light using the already described imaging sequence. For every measurement the HFI lasers are locked anew on the required VCO frequency and scanned by tuning the VCO for ca. 50 MHz over the transition in order to obtain the resonance frequency. This requires a calibration of the VCO set frequency versus the applied magnetic field strength.

Calibration of the high-field imaging setup

The HFI imaging setup has been calibrated by scanning both lasers for magnetic field strengths from 0 - 944 G. The optimal VCO value is determined by maximal absorption of atoms (resonance case). The obtained values for both laser locks are shown in Fig. 4.6. A linear fit to the data results in the following calibration:

$$\begin{aligned} \text{repumper} &: \nu_{\text{VCO,Rep}} [\text{MHz}] = 578(5) \text{ MHz} + B [\text{G}] \times 2.15(1) \text{ MHz/G} \\ \text{imaging} &: \nu_{\text{VCO,Img}} [\text{MHz}] = 793.5(4) \text{ MHz} + B [\text{G}] \times 1.408(1) \text{ MHz/G} \end{aligned}$$

The slope is consistent with the gradient of the Zeeman detuning for both HFI transitions, 2.12 MHz/G for the repumping and 1.40 MHz/G for the imaging transition (see Ch. 2). The frequency offsets of 793.5 MHz and 578 MHz in the calibration reduce the working regime of the HFI setup. This is due to the fact that the tuning range of the VCOs is limited by bandwidth of the frequency mixers, 2500 MHz for the imaging and 3000 MHz and the repumper setup, respectively. According to the upper expression the tuning range becomes smaller and hence the effective working regime. Therefore, the HFI system works up to magnetic fields of $B_{\max} \approx 1200$ G.

Effective absorption at high magnetic fields

Imaging at magnetic field leads to a reduced optical density. As explained in Sec. 4.1, this is due to the polarization of the imaging light. In our case the magnetic field is applied perpendicular to the imaging plane. Since σ^+ -light is used, the resonant cross section reduces to 1/4 of σ_0 , because only the projection onto the quantization axis is absorbed (see Eq. 4.10). This means one expects to observe a reduction of 75 % in absorption at high fields compared to imaging at zero magnetic field, which can be confirmed by the measurement depicted in Fig. 4.7. Each data point represents the peak optical density at resonance $od_{\max}(B)$ for a certain magnetic field strength B , which were obtained by a scan of the imaging laser (as described in Sec. 4.2). By reasons of time, only one scan was performed resulting in a lack of systematic errors. A drop of the absorption is clearly visible once a magnetic field is applied. With a linear fit to the data, a value of 0.15(1) is obtained, which corresponds to 26.9(2) % of the optical density compared to 0.54 at zero field.

Finally imaging of Cs atoms has been performed successfully at magnetic fields up to ~ 1000 G. A precise measurement is presented in Fig. 4.8, where absorption at a magnetic field strength of 870 G is shown. The imaging laser is locked here on a VCO frequency of 2025 MHz and the repumper laser on 2425 MHz, which corresponds to a frequency shift of 2091 MHz and 2354 MHz, respectively (confirmed by measurements of the beat signal). The magnetic field strength of 870 G is chosen, because of a zero-crossing of the Cs-Cs scattering length $a_{\text{Cs-Cs}}$. In this case the scattering between atoms reduces [32] and, hence, losses through three-body recombinations becomes smaller. Therefore, more atoms can be imaged. The imaging laser frequency is scanned few times over the resonance by ca. 40 MHz. The mean values with its statistical errors are fitted afterwards with a Voigt profile, which results in a FWHM $\Delta\omega_{\text{HFI},870\text{G}} \approx 8.1(2)$ MHz ($R^2 = 0.999$, $\chi^2_{\text{red}} = 1.033$). This is comparable to the FWHM $\Delta\omega_{\text{HFI},0\text{G}} \approx 8.0(2)$ MHz obtained by imaging at zero

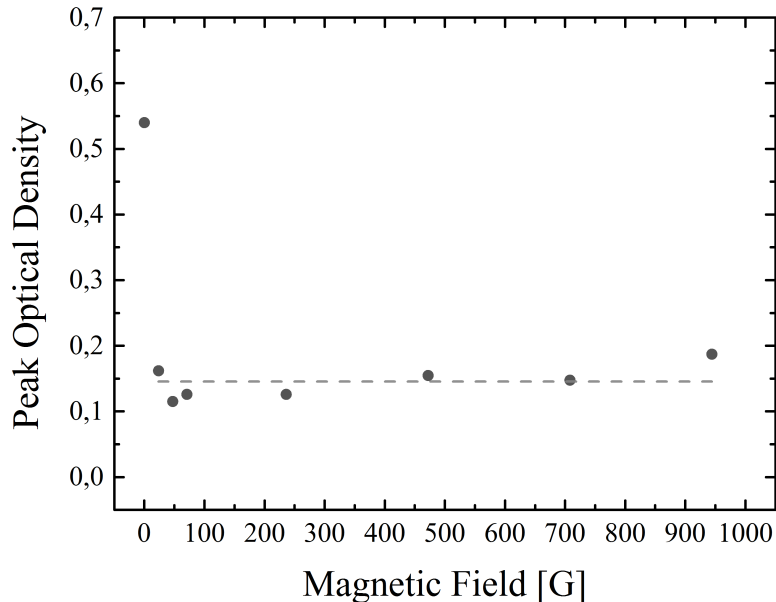


Figure 4.7: Optical density at different magnetic fields. The optical density drops to $\sim 26.9(2)\%$ to $\sim 0.15(1)$ compared to the value at zero field 0.54. A detailed explanation is given in the text.

field and gives rise to a consistent performance of the HFI system.

Drifts in long-term measurements

The stability of the HFI system has been also tested for long-terms (few hours). During the measurement the fluctuation in optical density and hence in atom number is ca. 5 %. Slow non-periodic drifts in optical density over few minutes (~ 4 min) are observable that corresponds to a decrease of 30 % in absorption. Simultaneously to the long-term measurement, the beat-note has been recorded by a spectrum analyzer. By comparing both measurements clear correlations are visible. The maximal drift in optical density relates to a drift of up to ~ 4 MHz in the beat-note's frequency, although the HFI lasers are locked and the beat-note's width does not fluctuate significantly over the whole measurement time. Disturbances by electronic components of the frequency offset lock can be excluded, since observed drifts here are much smaller $\Delta_{\text{drift}} \approx 200$ kHz < 4 MHz. Also other possible sources, e.g. heating effects in the delay line or a drift of the internal offset in the PID controller lie well below the observed results. Instabilities in the feedback loop can be also excluded, because the same drifts have been visible by using an improved

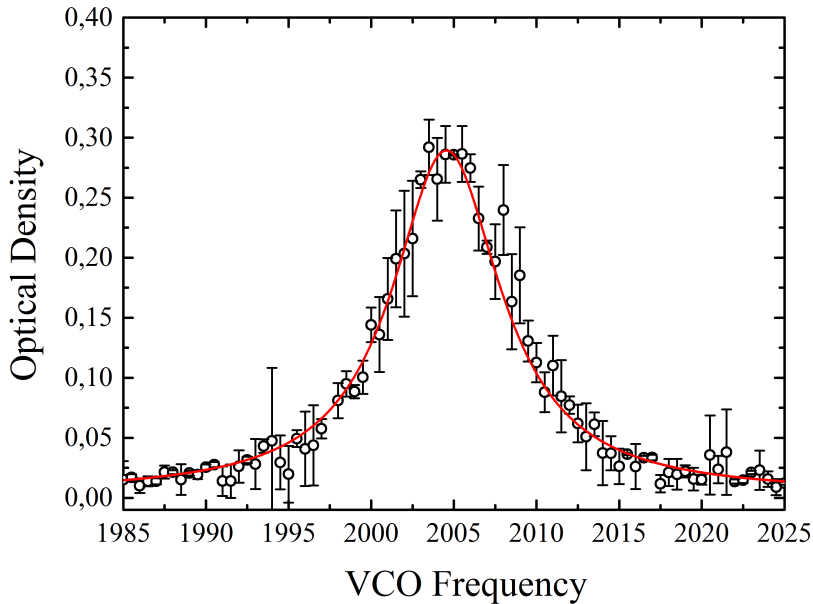


Figure 4.8: Scan of the imaging laser at 870 G. The data points describe the mean data over few scans and the error bars . The data is fitted with a Voigt profile (red line), resulting in a maximal absorption of 0.288(2) and a FWHM of $\Delta\omega_{\text{FWHM}} \approx 8.1(2)$ MHz.

version of PID controller⁸ for the frequency lock of the imaging laser. The drifts could be also due to drifts in the master laser frequency, since the high-field imaging laser is stabilized on it. But this could not be investigated until now. The drifts are still an open issue.

⁸ PID controller A 386 Na. It is designed and built by the electronics workshop of the Physikalisches Institut.

5. Conclusion and outlook

In the course of this thesis a system for imaging cesium in external magnetic fields was assembled, characterized and implemented in the main setup of the LiCs experiment. This required the installation of a new laser setup and the appropriate frequency stabilization. The laser setup consists of two DBR-lasers, one each for imaging and repumping, with a large frequency tuning range of ~ 27 GHz and a laser linewidth of ~ 6.2 MHz and ~ 14.1 MHz, respectively, which are offset locked on the main master lasers.

A detailed characterization and analysis of the frequency offset lock showed that its stability and the noise is basically dominated by the large laser linewidths. Long-term fluctuations are on the order of 1-2 MHz over 10 min and the noise spectrum depicted a level of $\sim 3 \times 10^5$ Hz²/Hz for the repumper and $\sim 6 \times 10^4$ Hz²/Hz for the imaging laser, respectively. This confirms the domination of the broad laser linewidths that gives an upper bound of stability. The influence of the broad width was also clearly visible in the imaging of cesium atoms. Since the imaging laser linewidth is larger than the natural linewidth of the D_2 -transition $\Gamma_{D_2} = 5.234$ MHz, the profile of the effective cross section becomes smaller and broader as predicted by a simulation and confirmed experimentally. By comparing the values of the FWHM with the low-field imaging system at zero-field, a reduction of about 40 % could be determined that yield a correction factor of 1.53(4) related to low-field imaging. Through a scan of the laser frequency over the imaging transition, broadening of the absorption profile could be further shown. A fit with a Voigt profile leads to a FWHM of 8.0(2) MHz.

Furthermore, imaging of cesium atoms at magnetic fields up to 1000 G was performed successfully. A detailed scan of the imaging laser at 870 G showed here a FWHM of 8.1(2) MHz that lies within the error of the value at zero field. It was further observed, that the optical density drops to about ~ 25 % relative to the zero-field, which is due to imaging with σ^+ -polarized light perpendicular to the quantization axis.

In order to further improve the imaging setup, a narrow-band laser with a linewidth of ~ 20 kHz $\ll \Gamma_{D_2}$ and a tuning range of 7 GHz was tested. The results demonstrated fluctuations on the order of ~ 30 kHz over 10 min, much smaller than with DBR lasers, and

5 Conclusion and outlook

a low noise performance of $\sim 4 \times 10^3 \text{ Hz}^2/\text{Hz}$. The measurement of the optical density would be therefore improved and hence the determination of the actual atom number, but with the constraint of a lower tunability, which would lead to imaging in a smaller range of accessible magnetic fields.

The results in this thesis show that high-field imaging of cesium atoms can be successfully realized with the implemented system. It allows one now to measure atom numbers at high magnetic fields. Furthermore imaging is now less influenced by technical disturbances, e.g. before, the magnetic coils had to be switched off for imaging, which induced mechanical vibrations on the setup and thus fringes on the final absorption image. With the high-field imaging setup, these vibrations can be heavily reduced, because now the magnetic field does not have to be switched off.

The found interspecies Feshbach resonances of ${}^6\text{Li}$ and ${}^{133}\text{Cs}$ offer prospects for the investigation of quantum phenomena, which could be observed with the high-field imaging, for example Li-Cs Feshbach molecules. These are weakly bound dimer states formed close to a Feshbach resonance. Since they are short-lived, the high-field imaging is here particularly advantageous, because the molecules, by means of the Cs atom, can be now observed without a time delay, which is generated by switching off the magnetic coils before.

Furthermore the two broad s-wave resonances at 843.5 G and 889.2 G [20] are favored for the observation of Cs-Cs-Li Efimov states [27], which describe three-body states. These can be measured by scanning the magnetic field close to a Feshbach resonance and searching for loss signatures, which are induced by recombination of trimers into a dimer and an atom with high kinetic energy. The Efimov state can be verified by determination of the three-body loss rate coefficient. This is done by observing the time evolution of the atom number at the specified signatures [26]. Moreover, the binding energies of Efimov states could be measured by RF-spectroscopy.

Appendix

A Atomic properties of Cs

Optical Properties		
wavelength(Vacuum)	λ	852.347 275 82(27) nm
natural linewidth	Γ	$2\pi \cdot 5.234(13)$ MHz
frequency	ω_0	$2\pi \cdot 351.72571850(11)$ THz
lifetime	τ	30.405(77) ns
Optical cycling transitions		
$ F = 4, m_F = \pm 4\rangle \rightarrow F' = 5, m'_F = \pm 5\rangle$		
saturation intensity	I_{sat}	1.1049(20) mW/cm ²
resonant absorption cross section	σ_0	$3.4687623065(15) \times 10^{-9}$ cm ²

Table A.1: Properties of the D₂ - transition $6^2S_{1/2} \rightarrow 6^2P_{3/2}$ and the optical cycling transition $|F = 4, m_F = \pm 4\rangle \rightarrow |F' = 5, m'_F = \pm 5\rangle$. All values are taken from [36].

Ground state $6^2S_{1/2}$		
magnetic dipole constant	A_{HFS}	$h \cdot 2298.157 942 5$ MHz
fine structure Landé g-factor	g_J	2.002 540 32(20)
hyperfine splitting	ΔE_{HFS}	$F = 3 \leftrightarrow F = 4$ $h \cdot 9.192 631 770$ GHz
Excited state $6^2P_{3/2}$		
magnetic dipole constant	A_{HFS}	$h \cdot 50.288 27(23)$ MHz
fine structure Landé g-factor	g_J	1.334 00(30)
hyperfine splitting	ΔE_{HFS}	$F = 2 \leftrightarrow F = 3$ $h \cdot 151.224 7(16)$ GHz
		$F = 3 \leftrightarrow F = 4$ $h \cdot 201.287 1(11)$ GHz
		$F = 4 \leftrightarrow F = 5$ $h \cdot 251.091 6(20)$ GHz
nuclear g-factor	g_I	-0.000 398 853 85(53)

Table A.2: Magnetic dipole constants, hyperfine energy splitting, fine structure and nuclear g-factor. All values are taken from [36].

Imaging transition			
$ I = 7/2, J = 1/2)F = 4, m_F = 4\rangle \leftrightarrow I' = 7/2, m'_J, J' = 3/2, m'_I, q\rangle$			
m'_I	m'_J	q	S_{rel}
7/2	-1/2	-1	1/12
7/2	1/2	0	1/6
7/2	3/2	1	1/4
$ I = 7/2, J = 1/2)F = 4, m_F = -4\rangle \leftrightarrow I' = 7/2, m'_J, J' = 3/2, m'_I, q\rangle$			
m'_I	m'_J	q	S_{rel}
-7/2	-3/2	-1	1/4
-7/2	-1/2	0	1/6
-7/2	1/2	1	1/12
Repumper transition			
$ I = 7/2, J = 1/2)F = 3, m_F = 3\rangle \leftrightarrow I' = 7/2, m'_J, J' = 1/2, m'_I, q\rangle$			
m'_I	m'_J	q	S_{rel}
5/2	-1/2	-1	1/24
5/2	1/2	0	1/48
7/2	-1/2	0	7/48
7/2	1/2	1	7/24
$ I = 7/2, J = 1/2)F = 3, m_F = 4\rangle \leftrightarrow I' = 7/2, m'_J, J' = 1/2, m'_I, q\rangle$			
m'_I	m'_J	q	S_{rel}
5/2	-1/2	-1	7/24
5/2	1/2	0	7/48
7/2	-1/2	0	1/48
7/2	1/2	1	1/24

Table A.3: S_{rel} of allowed transitions of the D_2 -line at high magnetic fields. The ground state is given in $|IJ)Fm_F\rangle$ and the excited state in $|I, m_I, J, m_J\rangle$, respectively. q describes the polarization of the light.

B Frequency offset lock with a narrow–band laser

The characterization of the laser system for high-field imaging in Ch. 3 shows that the stability is dominated by the laser linewidth. Also, the broad linewidth influences significantly the absorption imaging of cesium atoms, as described in Ch. 4. Therefore a narrow-band laser by RADIANT DYES (NarrowDiode, 852 nm) has been tested and compared with the existing high-field imaging system. For this purpose the beat-note¹ with the *master cooler* is detected on a fast photodiode (EOT ET-2030A, 1.2 GHz Bandwidth) and the laser is stabilized by frequency offset locking. For generating the error signal, the same electronic setup (see Fig. 3.7), as in Sec. 3.2, is implemented. For stabilization, however, a convenient commercial PID controller by RADIANT DYES is taken. The test setup is depicted in Fig. B.1. The system has been characterized the same way as the HFI system in Ch. 3 by means of beat-note’s width, long-term stability of the lock and the noise spectrum for a closed feedback loop. The measurements show that the narrow-band laser would highly increase the stability of the system and most likely improve the absorption imaging of cesium atoms at high magnetic fields.

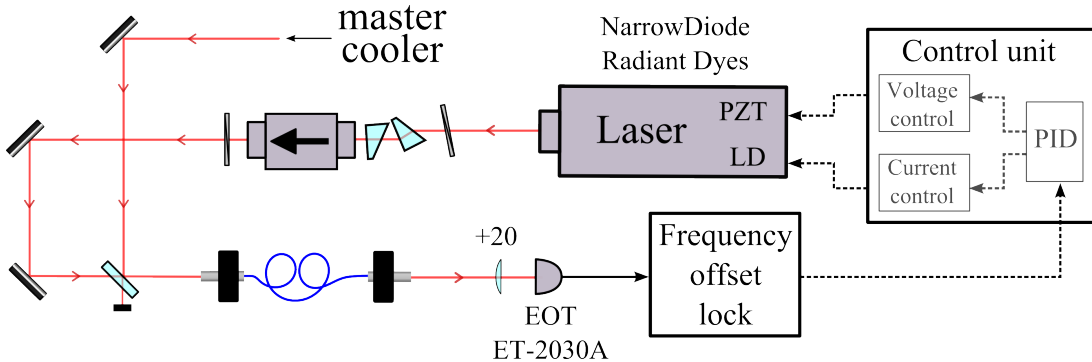


Figure B.1: Test setup for offset lock with the narrow diode laser by Radiant Dyes (NarrowDiode).

Interference-filter-stabilized ECDL

The laser setup is based on the design developed by the *Rosenbusch group* [60]. It follows the basic concept of an ECDL. But in contrast to the common used Littrow configuration [41], wavelength selectivity and control of the optical feedback are decoupled, which means both can be controlled independently. This is possible due to a narrow-band interference filter instead of a grating. Thus the external cavity is built on the same axis as a

¹ Both beams are coupled into a polarization maintaining fibre, where they are perfectly overlapped. Thus a beat-note is generated.

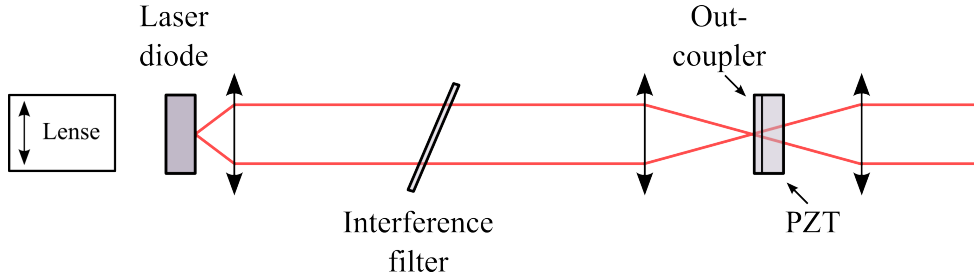


Figure B.2: Principle of the interference-filter-stabilized external cavity diode laser.
The figure is adapted from reference [60].

partially reflective out-coupler mounted on a piezo-electric transducer (PZT), with which the feedback into the laser diode is controlled (see Fig. B.2). The laser is specified with a linewidth² of ~ 20 kHz and a frequency tuning range of up to ~ 2 GHz, which makes this laser ideal for high-field imaging of cesium atoms.

Width of the beat-note

The width of the beat signal has been determined in the same way as in Sec. 3.2. The narrow-band laser is locked on a VCO frequency of 1000 MHz and the beat signal is measured with a spectrum analyzer, which is set to a resolution bandwidth (RBW) of 3 kHz and a sweep time (SWT) of 100 ms. The data are represented in Fig. B.3 and show the averaged beat note, where 100 traces were recorded consecutively. A fit to the data by a Gaussian distribution gives a FWHM of $\Delta\omega_{\text{FWHM}} = 202(2)$ kHz ($R^2 = 0.969$, $\chi^2 = 0.03$). This is much smaller than the widths of $\Delta\omega_{\text{FWHM,HFI}} = 6.23(5)$ MHz and 14.1(1) MHz obtained by the previous beat measurement with the imaging and the repumper laser, respectively. Because of the small laser linewidth of the narrow-band laser, it can be assumed that the FWHM of the beat signal is dominated by the width of the master laser, which is in this case the *master cooler* with a linewidth of ~ 200 kHz [39]. This means that the stability of the frequency offset lock would be dominated by the master laser's stabilization.

Long-term stability

The long-term stability of the frequency offset locking with the narrow-band laser has been tested by measuring the beat-note's frequency and its FWHM over few minutes by the same method as in Sec. 3.2. Every second a trace of the beat signals is recorded with

² The laser is sensitive on acoustical noise, which leads to a fast laser linewidth of about ~ 100 - 200 kHz [60].

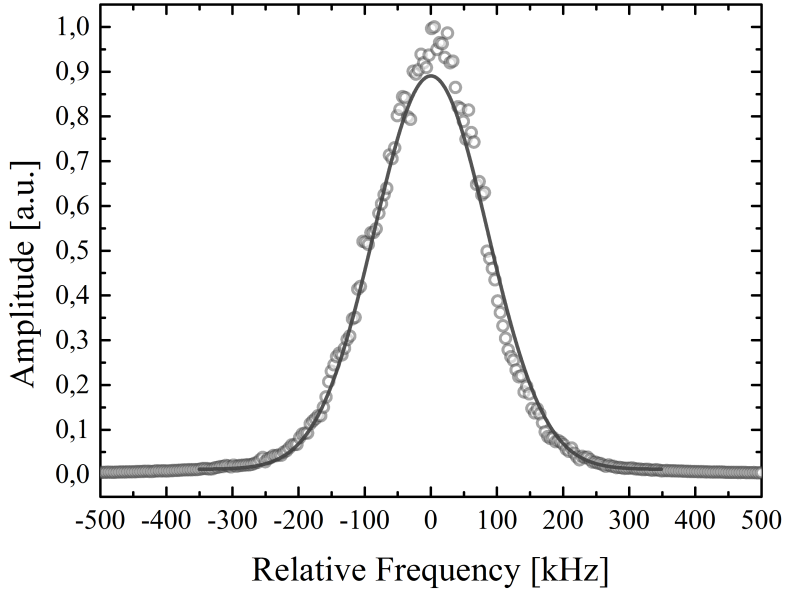


Figure B.3: Beat-note of the NarrowDiode with the *master cooler* in the locked state.

The data were fitted with a Gaussian profile resulting in a FWHM $\Delta\omega_{\text{FWHM}} \approx 202(2)$ kHz.

the spectrum analyzer (RBW: 3 kHz, SWT: 100 ms). Afterwards each trace is fitted with a Gaussian distribution, that gives the FWHM and the central beat frequency. In Fig. B.4 the fit results are plotted over time. By assuming a normal distribution of the data points, fluctuations³ of ~ 30 kHz relative to the mean beat frequency (934.49 MHz) and of ~ 34 kHz relative to the mean FWHM (186 kHz) can be estimated. These fluctuations are smaller than those (1 - 2 MHz) of the HFI lock and well below the natural linewidth of the D₂-transition. Also measurements over one hour show a smaller fluctuation of $\sim 100 - 200$ kHz.

Noise spectrum

The results in Sec. 4.3 show that, among other things, a good and efficient absorption imaging depends on the laser linewidth. Since it is strongly influenced by applied noise [50, 53], the noise spectrum has been investigated and compared with the existing HFI system. The noise spectrum has been obtained according to the method presented in Sec. 3.2. The measurement depicted in Fig. B.5 presents the case for a closed feedback loop. One can see

³ The fluctuations describe the FWHM of the normal distribution and not the standard deviation.

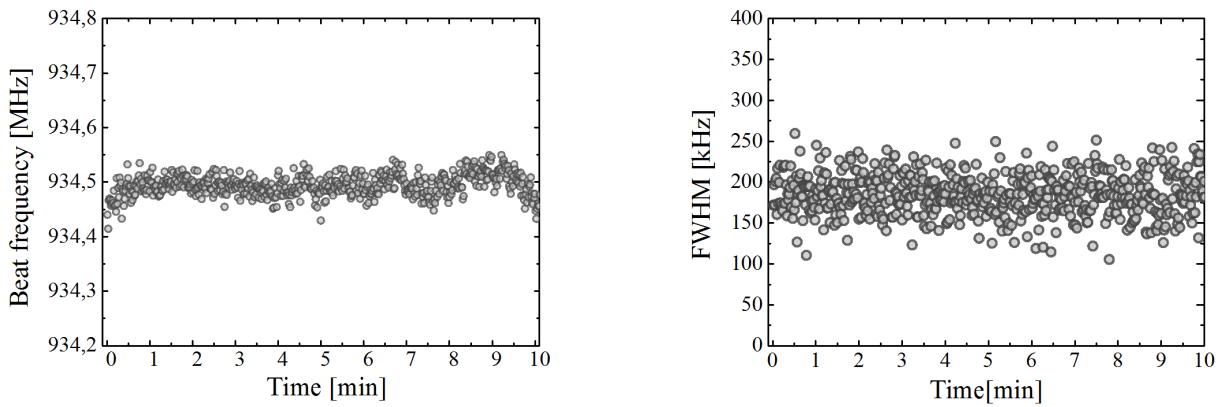


Figure B.4: Long-term fluctuations. (a) shows fluctuations of the beat-note's frequency and (b) of its linewidth given in FWHM according to a Gaussian profile.

that arbitrary noise is regulated up to ~ 1 MHz, which makes this system less insensitive on typical noise sources like e.g. mechanical vibrations ($\sim 1\text{--}100$ kHz) or power supplies ($\sim 40\text{--}60$ kHz) [49]. Furthermore it is noticeable that the noise level of $\sim 4 \times 10^3$ Hz²/Hz is almost one order of magnitude smaller than the frequency offset lock of the HFI lasers, which indicates a better performance of the frequency stabilization. Since this value is comparable with the noise level of the master laser's lock of $\sim 3 \times 10^3$ Hz²/Hz⁴ obtained by previous measurements [39], one can assume that the noise is basically influenced by the master laser's linewidth.

⁴ While measuring the beat signal, the master laser has been locked without using the high-frequent part of the injection current for stabilization.

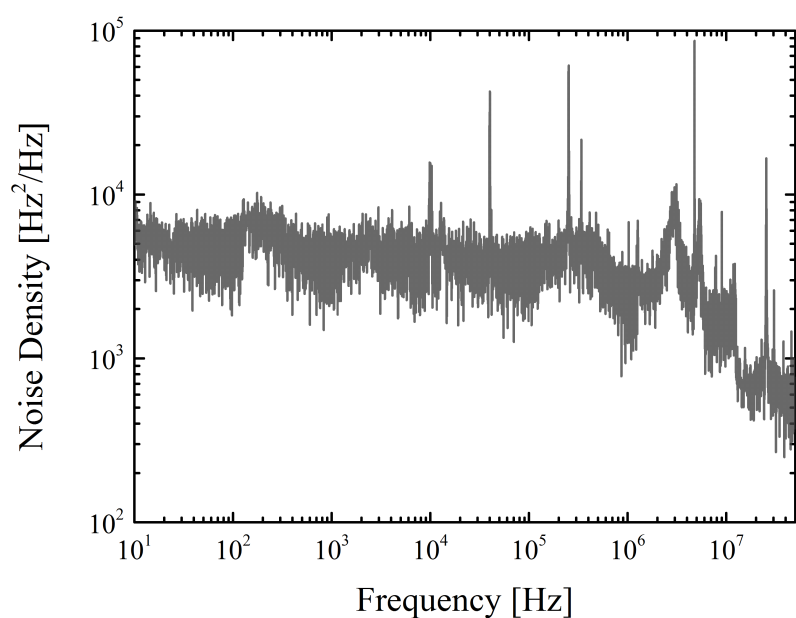


Figure B.5: Spectral noise density of the offset lock. The noise level lies at $\sim 5 \times 10^3 \text{ Hz}^2/\text{Hz}$ and is constant for frequencies up to 1 MHz indicating a stable frequency offset lock.

C Modulation transfer spectroscopy

In the course of this thesis, a new spectroscopy setup for locking the *master repumper* was assembled, the modulation transfer spectroscopy (MTS). This technique provides very stable locking, since it is independent on linear background absorption and hence less sensitive on experimental conditions. In the following first the basic principle as well as the experimental implementation will be briefly explained.

Basic concept

Modulation transfer spectroscopy (MTS) describes a pump-probe technique that allows to observe absorption of atomic transitions with a sub-Doppler resolution. Its basic principle is as follows. Pump and probe beam are aligned collinear through a vapor cell in counter-propagating directions as shown in Fig. C.1. The pump light is passed through an electro-optical modulator (EOM), which phase-modulates the pump beam with a frequency ω_m , so that the transmitted pump light is given by a carrier frequency ω_c with two sidebands ω_m [46]:

$$E(t) = E_0 \sin\{\omega_c t + \delta \sin(\omega_m t)\} , \quad (\text{C.1})$$

where δ describes the dimensionless modulation index. This expression can be rewritten to

$$E(t) = E_0 \left\{ \sum_{n=0}^{\infty} J_n(\delta) \sin((\omega_c + n\omega_m)t) + \sum_{n=1}^{\infty} (-1)^n J_n(\delta) \sin((\omega_c - n\omega_m)t) \right\} , \quad (\text{C.2})$$

with the Bessel function $J_n(\delta)$. The modulation is adjusted to a weak value, so that $\delta < 1$ and the resulting spectrum is dominated by the carrier frequency. When combining now both beams in the cesium cell, the probe beam is modulated for the case of a strong nonlinear interaction between both beams and the Cs atoms [46]. This is due to four-wave mixing, where three interacting waves can form a fourth wave as a result of the nonlinear susceptibility of the medium. In our case this means that the probe beam is mixed with the carrier and a sideband of the pump beam. Since this happens also for the other sideband of the pump beam, the probe beam is modulated with two sidebands. Both beat with the carrier and the resulting signal $S(\omega_m)$ is detected by a photodiode. In order to obtain a DC signal for the feedback loop, it is demodulated with a phase detector by means of mixing the beat signal $S(\omega_m)$ with ω_m . A detailed setup of the feedback loop for MTS is given in the diploma thesis of Stefan Schmidt [39]. Modulation transfer occurs only when both beams interact simultaneously with atoms that have the

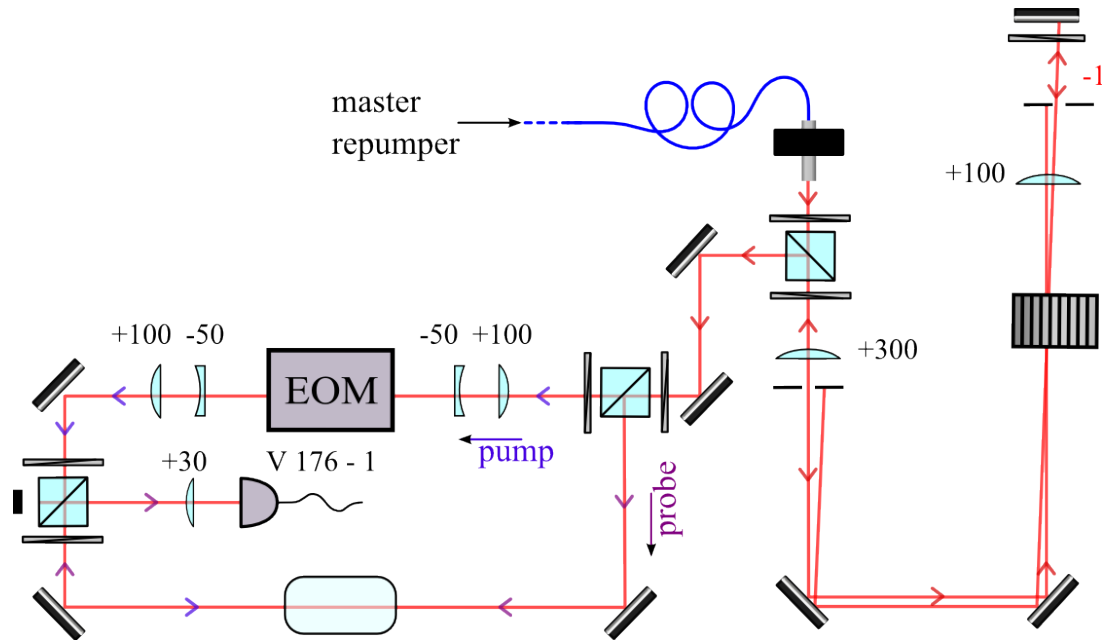


Figure C.1: Optical setup for the Modulation transfer spectroscopy.

same velocity (Doppler-free resonance condition), which makes it independent on linear absorption effects, e.g. Doppler-broadened background [61] resulting in a flat background of the error signal. Furthermore, four-wave mixing is most efficient for closed transitions, since atoms cannot decay into other states [46]. For this reason stabilization on the closed transition $F = 3 \rightarrow F' = 2$ should be implemented. However, this would mean that one also have to modify the actual optical setup, since the transition $F = 3 \rightarrow X_{34}$ has been used for locking the *master repumper* so far. In order to prevent this problem, an additional AOM has to be implemented, which shifts the light first by -250 MHz before it is used for MTS. Thus, locking on the closed transition $F = 3 \rightarrow F' = 2$ via MTS, results in a laser frequency, that is in resonance with $F = 3 \rightarrow X_{34}$.

Experimental implementation

The implemented setup is shown in Fig. C.1. The design follows the setup of the already installed MTS that is used for stabilization of the *master cooler* [39]. Light from the *master repumper*⁵ is guided through an optical fiber to the spectroscopy setup, so that ~ 1.06 mW is available. First the beam is guided through an AOM (CRYSTAL TECHNOLOGIES INC., 3120-198) in double-pass configuration, which shifts the light by -250 MHz. After passing the double-pass configuration the beam intensity reduces to ~ 550 μ W (double-

⁵ Settings for laser diode: injection current: 289 mA, temperature: 20.3 °C

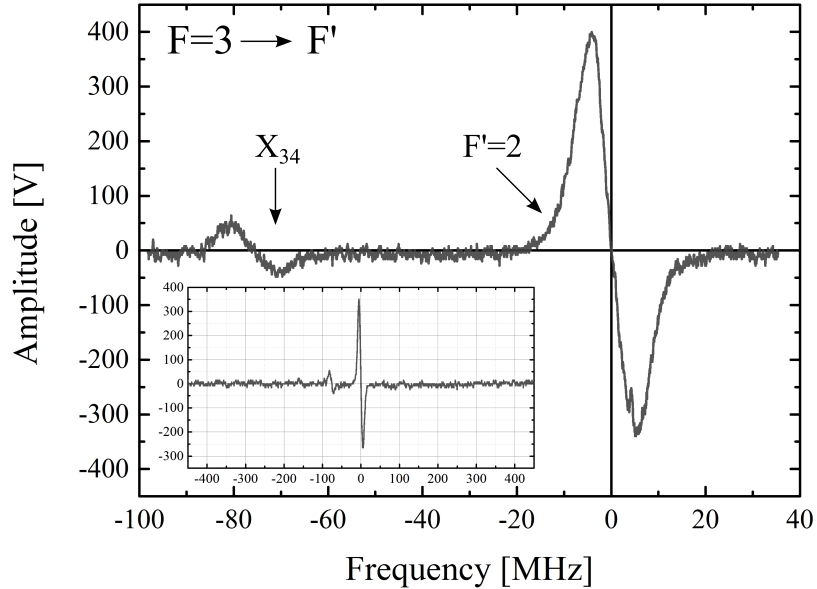


Figure C.2: Modulation transfer signal. The signal shows the transition from $F = 3 \rightarrow F'$. The strongest signal occurs for the closed transition $F = 3 \rightarrow F' = 2$, on which the spectrum is normalized.

pass efficiency: $\sim 55\%$) and with a polarizing beam splitter (PBS) the beam is divided into a pump and probe beam. With the $\lambda/2$ -waveplate in front of the PBS, the intensity of each beam is adjusted to an optimal error signal. According to reference [46], the modulation transfer signal has its maximum gradient, when the pump beam is modulated with a frequency approximately equal to the natural width of the D_2 -transition $\Gamma_{D_2} = 5.234$ MHz: $\omega_m/\Gamma \approx 1$. Therefore the EOM is driven with $\omega_m \approx 6$ MHz ($\omega_m/\Gamma \approx 1.2$), among others. The obtained error signal is depicted in Fig. C.2. It shows the spectrum for transitions from $F = 3$. One can see that for the closed transition $F = 3 \rightarrow F' = 2$ the strongest signal is generated. It has a gradient of ~ 133.1 mV/MHz. As expected a flat background can be observed. Laser stabilization on this signal has been tested successfully. The *master repumper* lock remained stable for few hours and did not show any drifts or fluctuations. In order to test the efficiency and quality of the stabilization, the spectral noise density has been measured (with the same method as described in Sec. 3.2.3), which is presented in Fig. C.3. It shows a low-noise level of 4×10^3 Hz 2 /Hz, which is comparable to the value that had been achieved by locking with the FMS before [39]. Moreover, one can observe that the feedback regulates noise up to $\sim 1 - 2$ kHz, where the servo bump occurs. This denotes a feedback bandwidth of few kHz, but in order to obtain

Appendix

a detailed value another method is needed, e.g. using a lock-in amplifier as described in Sec.3.2.3.

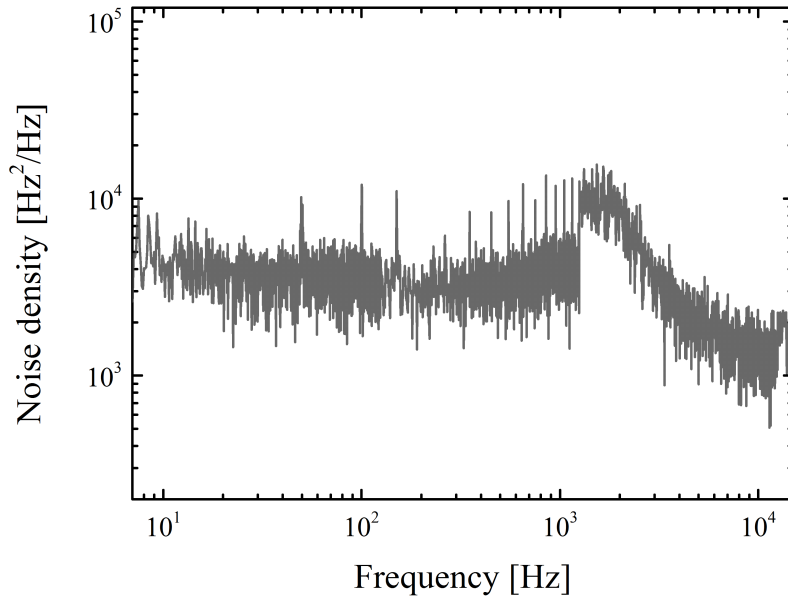


Figure C.3: Spectral noise density. The *master repumper* is locked here on the $F = 3 \rightarrow F' = 2$ via modulation transfer spectroscopy. The noise level lies at $4 \times 10^3 \text{ Hz}^2/\text{Hz}$ and is comparable with other locks used in the experiment [39, 51]. The large peak at $\sim 2 \text{ kHz}$ is the servo bump of the feedback loop (see Sec. 3.2.3), whereas the narrow peaks are due to a ground loop at 50 Hz and its multiples.

D Detailed overview of optical setup

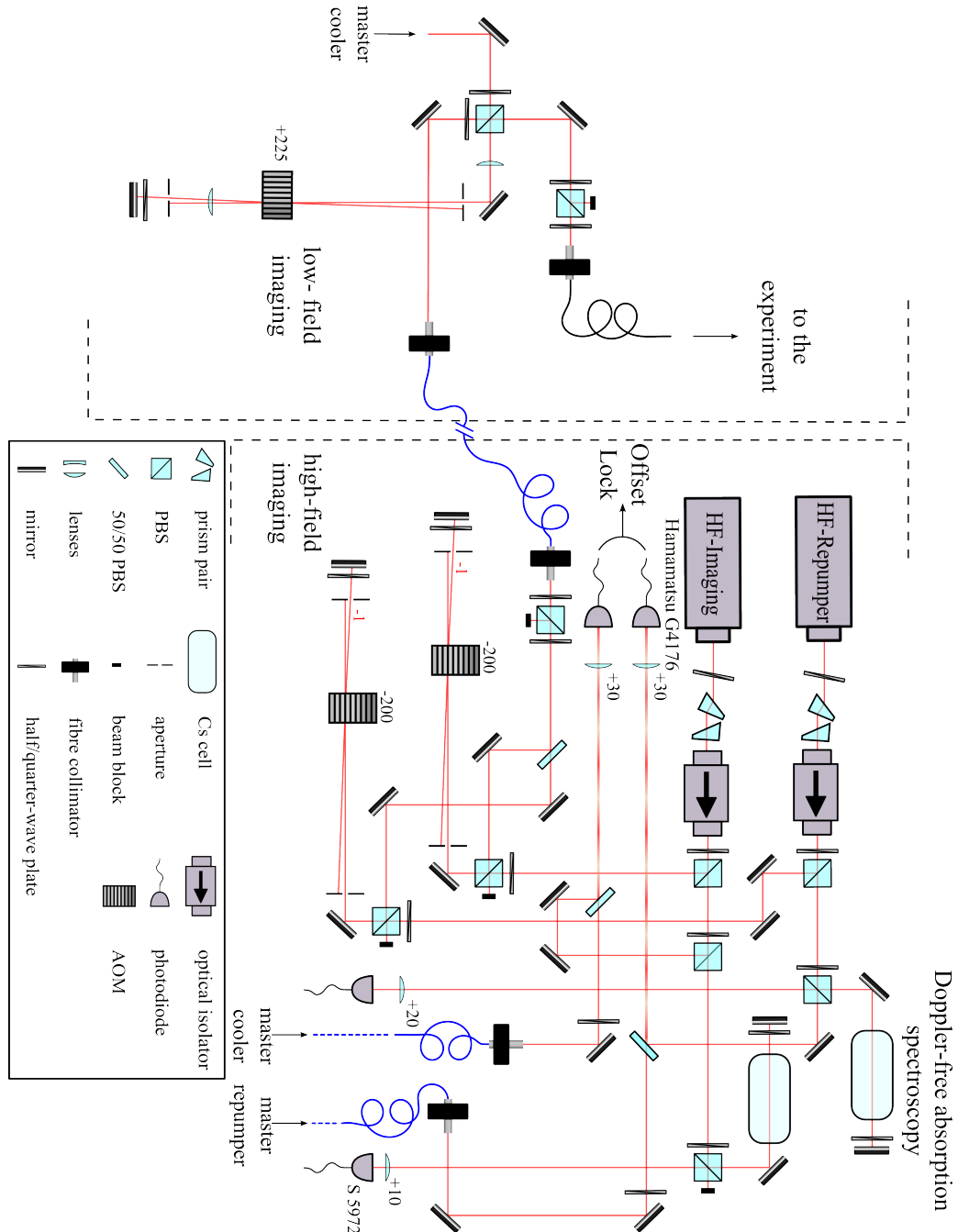


Figure D.1: Optical setup for high-field imaging. This figure shows a detailed overview of the optical setup as it is implemented in the experimental setup. The setup is similar to the illustrated in Fig. 3.4. An additional Doppler-free spectroscopy was also assembled to enable an easy adjustment of the laser frequency.

Bibliography

- [1] William D. Phillips and Harold Metcalf. Laser deceleration of an atomic beam. *Phys. Rev. Lett.*, 48(48):596, 1982.
- [2] S. N. Bose. *Z. Phys.*, 26:178, 1924.
- [3] Albert Einstein. Quantentheorie des einatomigen gases. *Sitzungsber. Preuss. Akad. Wiss.*, Bericht 3:18, 1925.
- [4] M. H. Anderson, J. R. Ensher, M. R. Matthews, C. E. Wiemann, and E. A. Cornell. Observation of bose-einstein condensation in a dilute atomic vapor. *Science*, 269:198–201, 1995.
- [5] K. B. Davis, M. O. Mewes, M. R. Andrews, N. J. van Druten, D. S. Durfee, D. M. Kurn, and W. Ketterle. Bose-einstein condensation in a gas of sodium atoms. *Phys. Rev. Lett.*, 75(22):3969 – 3973, 1995.
- [6] C.C.Bradley, C.A. Sackett, J.J. Tollett, and R.G. Hulet. Evidence of bose-einstein condensation in an atomic gas with attractive interactions. *Phys. Rev. Lett.*, 75(9):1687–1690, 1995.
- [7] B. DeMarco and D. S. Jin. Onset of fermi degeneracy in a trapped atomic gas. *Science*, 285:1703–1706, 1999.
- [8] Andrew G. Truscott, Kevin E. Stecker, William I. McAlexander, Guthrie B. Partridge, and Randall G. Hulet. Observation of fermi pressure in a gas of trapped atoms. *Science*, 291:2570–2572, 2001.
- [9] F. Schreck, L. Khaykovich, K. L. Corwin, G. Ferrari, T. Bourdel, J. Cubizolles, and C. Salomon. Quasipure bose-einstein condensate immersed in a fermi sea. *Phys. Rev. Lett.*, 87:080403, 2001.

BIBLIOGRAPHY

- [10] R. Grimm, M. Weidemüller, and Y. B. Ovchinnikov. Optical dipole traps for neutral atoms. *Advances In Atomic, Molecular, and Optical Physics*, 42(92):95, 2000.
- [11] S. Jochim, M. Bartenstein, A. Altmeyer, G. Heindl, S. Riedl, C. Chin, J. Hecker Denschlag, and R. Grimm. Bose-einstein condensation of molecules. *Science*, 302:2101–2103, 2003.
- [12] Markus Greiner, Cindy A. Regal, and Deborah S. Jin. Emergence of a molecular bose-einstein condensate from a fermi gas. *Nature*, 426:537, 2003.
- [13] M. W. Zwierlein, C. A. Stan, C. H. Schunck, S. M. F. Raupach, S. Gupta, Z. Hadzibabic, and W. Ketterle. Observation of bose-einstein condensation of molecules. *Phys. Rev. Lett.*, 91:250401, 2003.
- [14] Ph. Courteille, R. S. Freeland, D. J. Heinzen, F. A. van Abeelen, and B. J. Verhaar. Observation of a feshbach resonance in cold atom scattering. *Phys. Rev. Lett.*, 81:69, 1998.
- [15] S. Inouye, M. R. Andrews, J. Stenger, H.-J. Miesner, D. M. Stamper-Kurn, and W. Ketterle. Observation of feshbach resonances in a bose-einstein condensate. *Nature*, 392:151, 1998.
- [16] C. A. Stan, M. W. Zwierlein, C. H. Schunck, S. M. F. Raupach, and W. Ketterle. Observation of feshbach resonances between two different atomic species. *Phys. Rev. Lett.*, 93:143001, 2004.
- [17] S. Inouye, J. Goldwin, M. L. Olsen, C. Ticknor, J. L. Bohn, and D. S. Jin. Observation of heteronuclear feshbach resonances in a mixture of bosons and fermions. *Phys. Rev. Lett.*, 93:183201, 2004.
- [18] Francesca Ferlaino, Chiara D'Errico, Giacomo Roati, Matteo Zaccanti, Massimo Inguscio, Giovanni Modugno, and Andrea Simoni. Feshbach spectroscopy of a $k - rb$ atomic mixture. *Phys. Rev. A*, 73:040702, 2006.
- [19] T. Schuster, R. Scelle, A. Trautmann, S. Knoop, M. K. Oberthaler, M. M. Haverhals, M. R. Goosen, S. J. J. M. F. Kokkelmans, and E. Tiemann. Feshbach spectroscopy and scattering properties of ultracold li + na mixtures. *Phys. Rev. A*, 85:042721, 2012.

- [20] M. Repp, R. Pires, J. Ulmanis, R. Heck, E. D. Kuhnle, and M. Weidmüller. Observation of interspecies ${}^6\text{Li} - {}^{133}\text{Cs}$ feshbach resonances. *Phys. Rev. A*, 87(010701(R)):010701, 2013.
- [21] F. M. Cucchietti and E. Timmermans. Strong-coupling polarons in dilute gas bose-einstein condensates. *Phys. Rev. Lett.*, 96:210401, Jun 2006.
- [22] J. Tempere, W. Casteels, M. K. Oberthaler, S. Knoop, E. Timmermans, and J. T. Devreese. Feynman path-integral treatment of the bec-impurity polaron. *Phys. Rev. B*, 80:184504, Nov 2009.
- [23] J. Catani, G. Lamporesi, D. Naik, M. Gring, M. Inguscio, F. Minardi, A. Kantian, and T. Giamarchi. Quantum dynamics of impurities in a one-dimensional bose gas. *Phys. Rev. A*, 85:023623, Feb 2012.
- [24] V. Efimov. Weakly bound states of three resonantly-interacting particles. *Sov. J. Nuc. Phys.*, 12:589, 1971.
- [25] Eric Braaten and H.-W. Hammer. Efimov physics in cold atoms. *Annals of Physics*, 322:120, 2007.
- [26] F. Ferlaino, A. Zenesini, M. Berninger, B. Huang, H.-C. Nägerl, and R. Grimm. Efimov resonances in ultracold quantum gases. *Few-Body Systems*, 51:113, 2011.
- [27] J. P. D’Incao and B. D. Esry. Mass dependence of ultracold three-body collision rates. *Phys. Rev. A*, 73:030702, Mar 2006.
- [28] U. Schünemann, H. Engler, R. Grimm, M. Weidmüller, and M. Zielinkowski. Simple scheme for tunable frequency offset locking of two lasers. *Rev. Sci. Instrum.*, 70(1):242–243, 1999.
- [29] G. Ritt, G. Cennini, C. Geckeler, and M. Weitz. Laser frequency offset locking using a side if filter technique. *Applied Physics B*, 79:363–365, 2004.
- [30] G. Puentes. Laser frequency offset locking scheme for high-field imaging of cold atoms. *Appl. Phys. B*, 107:11–16, 2012.
- [31] M. Berninger, A. Zenesini, B. Huang, W. Harm, H.-C. Nägerl, F. Ferlaino, R. Grimm, P. S. Julienne, and J. M. Hutson. Universality of the three-body parameter for efimov states in ultracold cesium. *Phys. Rev. Lett.*, 107:120401, 2011.

BIBLIOGRAPHY

- [32] Martin Berninger, Alessandro Zenesini, Bo Huang, Walter Harm, Hanns-Christoph Nägerl, Francesca Ferlaino, Rudolf Grimm, Paul S. Julienne, and Jeremy M. Hutson. Feshbach resonances, weakly bound molecular states, and coupled-channel potentials for cesium at high magnetic fields. *Phys. Rev. A*, 87:032517, 2013.
- [33] Ingolf V. Hertel and Claus-Peter Schulz. *Atome, Moleküle und optische Physik 1*, volume 1. Springer-Verlag Berlin Heidelberg, 2008.
- [34] Herrman Haken and Hans Christoph Wolf. *Atom- und Quantenphysik*, volume 8. Springer-Verlag Berlin Heidelberg, 2004.
- [35] G. Breit and I. I. Rabi. Measurement of nuclear spin. *Physical Review*, 38(2082), 1931.
- [36] Daniel Adam Steck. *Cesium D Line Data*. <http://steck.us/alkalidata>, 2010.
- [37] Martin Berninger. *Universal three- and four-body phenomena in an ultracold gas of cesium atoms*. PhD thesis, University of Innsbruck, 2011.
- [38] Dmitry Budker, Derek F. Kimball, and David P. DeMille. *Atomic Physics - An Exploration through Problems and Solutions*, volume 2. Oxford University Press, 2008.
- [39] Stefan M. W. Schmidt. Aufbau und charakterisierung eines frequenzstabilisierten diodenlasersystems zur kühlung und speicherung von cs-atomen. Master's thesis, Universität Heidelberg, 2011.
- [40] Marc Repp. *Interspecies Feshbach Resonances in an Ultracold, Optically trapped Bose-Fermi Mixture of Cesium and Lithium*. PhD thesis, University of Heidelberg, 2013.
- [41] L. Ricci, M. Weidemüller, T. Esslinger, A. Hemmerich, C. Zimmermann, V. Vuletic, W. König, and T. W. Hänsch. A compact grating-stabilized diode laser system for atomic physics. *Optics Communications*, 117:541–549, 1995.
- [42] Stefan Spießberger. *Compact Semiconductor-Based Laser Sources with Narrow Linewidth and High Output Power*. PhD thesis, Technische Universität Berlin, April 2012.
- [43] Bahaa E. A. Saleh and Malvin Carl Teich. *Fundamentals of Photonics*, volume 2. Wiley-Interscience, John Wiley & Sons, Inc., 2007.

- [44] Dieter Meschede. *Optik, Licht und Laser*, volume 3. Vieweg + Teubner, 2008.
- [45] Ferdinand-Braun-Institut. Durchstimmbare mehrsektionslaser mit internen wellenlängenselektivem reflektor (dbr-laser). July 2013.
- [46] D. J. McCarron, S. A. King, and S. L. Cornish. Modulation transfer spectroscopy in atomic rubidium. *Meas. Sci. Technol.*, 19(105601):105601, 2008.
- [47] E. A. Donley, T. P. Heavner, F. Levi, M. O. Tataw, and S-R-Jefferts. Double-pass acoustic-optic modulator system. *Rev. Sci. Instrum.*, 76:063112, 2005.
- [48] Paul Horowitz and Winfried Hill. *The Art of Electronics*. Cambridge University Press, 2 edition, 1989.
- [49] Matthias Weidmüller and Claus Zimmermann. *Interactions in Ultracold Gases - From Atoms to Molecules*. Wiley-VCH Verlag, 2003.
- [50] Stefan Kunze, Steffen Wolf, and Gerhard Rempe. Measurement of fast frequency fluctuations: Allan variance of grating-stabilized diode laser. *Optics Communications*, 128:269–274, 1996.
- [51] Romain Müller. Optical cooling and trapping of fermionic ^6Li and bosonic ^{133}Cs . Master’s thesis, University of Heidelberg, 2011.
- [52] D. S. Elliot, Roy Rajarshi, and S. J. Smith. Extracavity laser-band shape and bandwidth modification. *Phys. Rev. A*, 26(1):12–18, 1982.
- [53] Gianni Di Domenico, Stephan Schilt, and Pierre Thomann. Simple approach to the relation between laser frequency noise and laser line shape. *Applied Optics*, 49(25):4801–4807, 2010.
- [54] W. Ketterle, D.S. Durfee, and D.M. Stamper-Kurn. Making, probing and understanding bose-einstein condensates. In S. Stringari M. Inguscio and C.E. Wieman, editors, *Varenna lecture notes, In Bose-Einstein condensation in atomic gases, Proceedings of the International School of Physics "Enrico Fermi"*, Course CXL, pages 67–176. IOS Press, Amsterdam, 1999.
- [55] J. J. Olivero and R. L. Longbothum. Empirical fits to the voigt line width: A brief review. *J. Quant. Spectrosc. Radiat. Transfer*, 17:233–236, 1977.
- [56] H. J. Metcalf and P. van der Straten. Laser cooling and trapping of atoms. *J. Opt. Soc. Am. B*, 20(887):887, 2003.

BIBLIOGRAPHY

- [57] M. Drewsen, Ph. Laurent, A. Nadir, G. Santarelli, A. Clairon, Y. Castin, D. Grison, and C. Salomon. Investigation of sub-doppler cooling effects in a cesium magneto-optical trap. *Applied Physics B*, 59:283, 1994.
- [58] A. Kerman, J. Vuletić, C. Chin, and S. Chu. Beyond optical molasses: 3d raman sideband cooling of atomic cesium to high phase space density. *Phys. Rev. Lett.*, 84:439, 2000.
- [59] Robert Heck. All-optical formation of an ultracold gas of fermionic lithium close to quantum degeneracy. Master's thesis, University of Heidelberg, 2012.
- [60] X. Baiillard, A. Gauguet, S. Bize, P. Lemonde, Ph. Laurent, A. Clairon, and P. Rosenbusch. Interference-filter-stabilized external-cavity diode lasers. *Optics Communications*, 266:609–613, 2006.
- [61] Wolfgang Demtröder. *Laserspektroskopie*, volume 5. Springer-Verlag Berlin Heidelberg, 2007.

Danksagungen

An dieser Stelle möchte ich mich bei all denjenigen bedanken, die mich während meiner Studienzeit begleitet und zum Gelingen dieser Arbeit beigetragen haben.

Zu allererst möchte ich mich bei Prof. Matthias Weidemüller bedanken. Durch die Aufnahme in seine Gruppe ermöglichte er es mir an einem spannenden Experiment und in einem hervorragenden Umfeld zu arbeiten. Es war wirklich eine tolle und lehrreiche Zeit. Auch möchte ich ihm für seine Unterstützung in schweren Zeiten während des Studiums danken.

Des Weiteren danke ich Prof. Selim Jochim für die Übernahme der Zweitkorrektur dieser Masterarbeit. An dieser Stelle möchte auch seiner Arbeitsgruppe für die gute Zusammenarbeit und die gegenseitige Unterstützung danken.

Ein ganz großer Dank geht an das Mixtures-Team. Insbesondere Eva Kuhnle, die die Betreuung dieser Arbeit übernahm. Für die vielen Diskussionen, deine stetige Unterstützung und die vielen motivierenden Worte, vor allem zum Ende dieser Masterarbeit, danke ich Dir wirklich sehr. Bedanken möchte ich mich auch bei Rico Pires, Marc Repp und Juris Ulmanis. Es war mir stets ein Vergnügen mit euch im Labor zu arbeiten. Durch die zahlreichen Diskussionen und eure Erfahrungen habe ich sehr viel gelernt, auch über die Physik hinaus. Meinen Mitstreitern Alda Arias Suarez und Stephan Häfner danke ich für die tolle Zusammenarbeit und die gegenseitige Unterstützung, genauso wie Robert Heck, der noch zu Beginn dieser Arbeit am Mixtures – Experiment mitwirkte. Auch möchte ich mich für die Zeit außerhalb des Labors bedanken.

Bastian Höltkemeier und Simone Götz danke ich für die vielen Gespräche, hilfreiche Tipps und die gemeinsame Stunden im und außerhalb des Büros. Den restlichen Mitgliedern des Motrims-Experiments, Julian Glässel und Henry Lopez, danke ich für die gegenseitige Unterstützung.

Bedanken möchte ich mich auch bei dem Rydberg-Team Shannon Whitlock, Martin Robert-de-Saint-Vincent, Christoph Hofmann, Georg Günter, Hanna Schempp, Vladislav Gavryusev und Stephan Helmrich für die gute Zusammenarbeit und die vielen Gefechte am Kicker-Tisch.

Von ganzem Herzen möchte ich mich bei meiner Familie bedanken. Ihr habt mich von Beginn an, bei allen meinen Entscheidungen unterstützt und mir immer den nötigen Rückhalt gegeben. Auch in schweren Zeiten konnte ich mich immer auf euch verlassen. Vielen Dank!

Zum Schluss möchte ich mich bei meiner Freundin Catrin bedanken. Durch ihren Glauben an meine Fähigkeiten, ihre Geduld und ihre Unterstützung, hat sie unbewusst zu einem Großteil dieser Arbeit beigetragen. Ich danke Dir sehr!

Erklärung:

Ich versichere hiermit, daß ich diese Arbeit selbstständig verfaßt und keine anderen als die angegebenen Quellen und Hilfsmittel benutzt habe.

Heidelberg, den

.....
(Unterschrift)